Hypoxia Promotes Breast Cancer Cell Growth by Activating a Glycogen Metabolic Program

Ke Tang[1], Liyan Zhu[1], Jie Chen[2], Dianheng Wang[1], Liping Zeng[1], Chen Chen[1], Liang Tang[1], Li Zhou[1], Keke Wei[1], Yabo Zhou[2], Jiadi Lv[2], Yuying Liu[2], Huafeng Zhang[3], Jingwei Ma[4], and Bo Huang[1,2]

ABSTRACT

Hypoxia is known to be commonly present in breast tumor microenvironments. Stem-like cells that repopulate breast tumors, termed tumor-repopulating cells (TRC), thrive under hypoxic conditions, but the underlying mechanism remains unclear. Here, we show that hypoxia promotes the growth of breast TRCs through metabolic reprogramming. Hypoxia mobilized transcription factors HIF1α and FoxO1 and induced epigenetic reprogramming to upregulate cytosolic phosphoenolpyruvate carboxykinase (PCK1), a key enzyme that initiates gluconeogenesis. PCK1 subsequently triggered retrograde carbon flow from gluconeogenesis to glycogenesis, glycogenolysis, and the pentose phosphate pathway. The resultant NADPH facilitated reduced glutathione production, leading to a moderate increase of reactive oxygen species that stimulated hypoxic breast TRC growth. Notably, this metabolic mechanism was absent in differentiated breast tumor cells. Targeting PCK1 synergized with paclitaxel to reduce the growth of triple-negative breast cancer (TNBC). These findings uncover an altered glycogen metabolic program in breast cancer, providing potential metabolic strategies to target hypoxic breast TRCs and TNBC.

Significance: Hypoxic breast cancer cells trigger self-growth through PCK1-mediated glycogen metabolism reprogramming that leads to NADPH production to maintain a moderate ROS level.

Introduction

The median oxygen partial pressure is around 10 mm Hg in most solid tumors, which is 4 to 6 folds lower than that in normal tissues (1, 2). This intratumoral hypoxia profoundly affects tumor cell behaviors and is a critical driving force behind cancer progression (3–5). In fact, tumor hypoxia is commonly associated with increased metastasis and a worse prognosis in patients with cancer (6, 7). Notwithstanding the paramount importance of hypoxia in tumor microenvironments, molecular mechanisms by which hypoxia remodels tumor cell behaviors remain vague. It is established that hypoxia reprograms the metabolic mode of tumor cells by increasing glycolysis and decreasing oxidative phosphorylation, as evidenced by the upregulation of key glycolytic genes such as glucose transporter 1 (GLUT1), hexokinase 2 (HK2), and lactate dehydrogenase A (LDHA)

in hypoxic tumor cells (8–10). Notably, hypoxia also triggers glycogen synthesis in hypoxic tumor cells (11–13). As an anabolic reaction process, glycogenesis is inverse to glycolytic catabolism. It has been reported that inflammatory macrophages degrade glycogen to generate G6P, which is channeled through the pentose phosphate pathway (PPP), leading to the generation of NADPH, a crucial molecule that is used to reduce oxidized glutathione (14). Meanwhile, glyceraldehyde 3-phosphate (G3P) and fructose 6-phosphate (F6P) as the end products of the PPP can enter the glycolysis for ATP production, thus reconciling catabolic glycolysis and anabolic glycogenesis during hypoxia. However, the mechanisms behind how hypoxia triggers glycogen synthesis in tumor cells remain unclear.

Despite the profound influence of hypoxia on tumor cells, distinct tumor cell subsets may respond differently. Indeed, breast tumor-repopulating cells (TRC) thrive and grow rapidly under hypoxia; in contrast, hypoxic differentiated tumor cells are growth retarded and even prone to undergo apoptosis (5). Cells usually mobilize gluconeogenesis to adapt to hypoxia (15, 16), which is the reverse process of glycolysis and has an inhibitory effect on glycolysis (17). This gluconeogenic pathway is hijacked by TRCs and allows a retrograde glucose carbon flow to serine and glycerol-3-phosphate, thus facilitating TRC growth (18, 19). Furthermore, such retrograde glucose carbon flow can be guided to glycogen synthesis and degradation, as evidenced in CD8+ memory T cells (20). Thus, it is likely that gluconeogenesis, glycogen metabolism, and glycolysis are orchestrated in TRCs to survive from the hostile hypoxia. In this study, we provide evidence that highly tumorigenic breast TRCs adapt to hypoxia through a gluconeogenesis-guided glycogen metabolic program, which moderately elevates ROS levels and promotes TRC growth.

Materials and Methods

Animals

Female 6- to 8-week-old BALB/C nude mice were purchased from the Center of Medical Experimental Animals of the Chinese Academy

[1]Department of Biochemistry and Molecular Biology, Tongji Medical College, Huazhong University of Science & Technology, Wuhan, China. [2]Department of Immunology, Institute of Basic Medical Sciences & State Key Laboratory of Medical Molecular Biology, Chinese Academy of Medical Sciences and Peking Union Medical College, Beijing, China. [3]Department of Pathology, Tongji Medical College, Huazhong University of Science & Technology, Wuhan, China. [4]Department of Immunology, Tongji Medical College, Huazhong University of Science & Technology, Wuhan, China.

Corresponding Author: Bo Huang, Department of Immunology, Institute of Basic Medical Sciences, Chinese Academy of Medical Sciences, Peking Union Medical College, No. 5, Dongdan Santiao, Beijing 100005, P.R. China. Phone: 8610-6915-6464; E-mail: tjhuangbo@hotmail.com

of Medical Science (CAMS, Beijing, China). All studies involving mice were approved by the Animal Care and Use Committee of Tongji Medical College (Wuhan, China).

Cell lines and culture

All human breast cancer cell lines (MCF7, T47D, SUM159) used in this study were purchased from the China Center for Type Culture Collection. MCF7 cells were cultured in DMEM (Thermo Fisher Scientific); T47D cells were cultured in RPMI1640 medium supplemented with 0.2 U/mL insulin; SUM159 cells were cultured in DMEM supplemented with 1.0 μg/mL hydrocortisone and 0.2 U/mL insulin. All media are supplemented with 10% fetal bovine serum (FBS; Gibco). All cells were maintained at 37°C in a humidified atmosphere containing 5% CO_2 and 95% N_2. Bulk cells or TRCs were cultured either under a normoxic condition (37°C, 5% CO_2, 21% O_2) or in a hypoxic chamber (37°C, 5% CO_2, 1% O_2). Cells have been tested for *Mycoplasma* detection, interspecies cross-contamination, and authenticated by isoenzyme and short tandem repeat (STR) analyses in the Cell Resource Centre of Peking Union Medical College (Beijing, China).

Human samples

Resected human breast cancer tissues were obtained from patients at Tongji Hospital (Wuhan, China) or National Cancer Center/Cancer Hospital (Beijing, China). Ethical permission was granted by the Clinical Trial Ethics Committee of Tongji Hospital or National Cancer Center/Cancer Hospital. All patients provided written informed consent to participate in the study.

Tumor models

Tumor models were conducted as described previously (5). After undergoing a two-day adaptation period, mice were used for studies. 5×10^6 MCF7 or T47D cells were inoculated into the mammary gland of nude mice. After the tumor grew up to 50 mm³, mice were followed by intragastric administration of 60 mg/kg sunitinib per day for 35 days. Then, mice were sacrificed, ALDH1^high and ALDH1^low tumor cells were sorted from breast tumor tissue by Aldefluor assay.

In PCK1 knockdown or overexpression tumor model, 1×10^6 *PCK1*-SGs- or *PCK1*-overexpressing MCF7 TRCs were inoculated into the mammary gland of nude mice (MCF-TRC transfected with control vector as control group).

In 3-MPA treatment tumor model, 1×10^6 MCF7 TRCs were inoculated into the mammary gland of nude mice. Meanwhile, mice were randomly divided into two groups and administered intragastrically with 3-MPA (30 mg/kg) or saline control for 4 weeks.

In combined treatment tumor model, 1×10^6 SUM159 TRCs were inoculated into the mammary gland of nude mice. Then, mice were randomly divided into four groups and were intraperitoneally injected with 10 mg/kg paclitaxel (once per week), or intragastrically administered 30 mg/kg 3-MPA or saline control for 4 weeks.

3D fibrin gel cell culture of tumor cells

TRC culture was conducted according to our previously described methods (21–23). In brief, tumor cells were maintained in the conventional rigid plate. After 0.25% trypsin digestion, cells were detached and suspended in DMEM or RPMI1640 medium (10% FBS), and cell density was adjusted to 10^4 cells/mL. Fibrinogen (Searun Holdings Company) was diluted into 2 mg/mL with T7 buffer (50 mmol/L Tris, 150 mmol/L NaCl, pH 7.4). A mixture was made by mixing the same volume of the fibrinogen solution and the cell solution, resulting in

1 mg/mL fibrinogen and 5,000 cells/mL in the mixture. Two hundred and fifty microliter cells per fibrinogen mixtures were seeded into each well of a 24-well plate mixed well with preadded 5 μL thrombin (0.1 U/mL, Searun Holdings Company). The cell culture plate was then moved into 37°C cell culture incubator incubated for 30 minutes. Finally, 1 mL DMEM or 1640 medium containing 10% FBS was added. On day 5, the cells cultured in soft 3D fibrin gels (90 Pascal) were treated with dispase II (Roche) for 10 minutes at 37°C, and then, the spheroids were collected and pipetted to single cells. In all experiments, TRCs were cultured and selected from 90 Pa soft 3D fibrin gels and bulk tumor cells were cultured in conventional rigid dish as control.

Periodic acid Schiff staining

Glycogen was detected in cells following a standardized periodic acid Schiff (PAS) staining technique. Briefly, cells were fixed with 4% paraformaldehyde for 15 minutes, incubated in 1% periodic acid (Sigma-Aldrich) for 5 minutes, rinsed in water, and placed in Schiff's reagent (Sigma-Aldrich) for 10 minutes. Finally, cells were washed with water. Images were obtained using a microscope.

Glycogen quantification

Glycogen levels were measured using the Glycogen Assay Kit (Abnova) following the manufacturer's instructions. Briefly, 1×10^6 cells were homogenized with 200 μL H_2O on ice and then boiled for 10 minutes. Homogenates were spun at $20,000 \times g$ for 10 minutes, and supernatants were assayed for glycogen content. Results were normalized by protein content.

Glycogen tracing assay

For ^{13}C glycogen or ^{13}C pyruvate tracing experiments, cells were treated with hydrochloric acid to degrade polymer glycogen into monomer glucose (24). Briefly, cell pellets were washed twice with PBS; then, 50 μL 6 N HCl was added for 30 minutes at 30°C. Subsequently, 250 μL water was added to the samples to dilute the acid to 1 N HCl and mixed by pipetting, then incubated at 110°C for 1 hour. After centrifugation briefly ($14,000 \times g$, room temperature, 30 seconds), 40 μL 5 N NaOH was added to the samples to neutralize the reaction and mixed by pipetting. Finally, the samples were evaporated to dryness at 65°C under a constant stream of air, then 50 μL 80% methanol/water was added to the dry samples. After centrifugation at $13,000 \times g$, 10 minutes at 4°C, supernatant extracts were analyzed by LC-MS as described previously.

Transmission electron microscopy

Bulk cells and TRCs under hypoxia were washed with PBS three times, then fixed in 4% glutaraldehyde in 0.1 mol/L PBS and processed for routine electron microscopy as described previously. Briefly, the samples were post fixed in 1% osmium tetroxide (OsO_4) for 100 minutes at room temperature, and rinsed with distilled water three times. The pellets were then dehydrated in a graded ethanol series, treated with propylene oxide, and embedded with Spurr's epoxy resin. Cut sections were stained with uranyl acetate and lead citrate, and then imaged using a JEM1010 electron microscope (JEOL).

Aldefluor assay and flow cytometry

Tumor tissues were digested and the single-cell suspension was obtained. The ALDH$^+$ cells were sorted by using ALDE-FLUOR Kit (STEM CELL Technologies) according to the supplier's instructions.

^{13}C tracing by liquid chromatography Q-exactive mass spectrometry

For ^{13}C tracing experiments, MCF7 bulk cells or TRCs were cultured under normoxia (21% O_2) and hypoxia (1% O_2). On day 4 of culture, cells were washed, then cultured with [U6]-^{13}C glucose, [U5]-^{13}C glutamine, [U3]-^{13}C pyruvate, or [U2]-^{13}C acetate (Sigma-Aldrich) for another 24 hours. Cells were washed twice in saline and lysed in extraction solvent (80% methanol/water) for 30 minutes at $-80°$C. After centrifugation at $13,000 \times g$, 10 minutes at $4°$C, supernatant extracts were analyzed by liquid chromatography Q-exactive mass spectrometry (LC-QE-MS) as described previously (5). In brief, liquid chromatography was performed using a HPLC (Ultimate 3000 UHPLC) system (Thermo Fisher Scientific) equipped with an Xbridge amide column (100 × 2.1 mm i.d, 3.5 μmol/L; Waters). The column temperature was maintained at $10°$C. The mobile phase A is 20 mmol/L ammonium acetate and 15 mmol/L ammonium hydroxide in water with 3% acetonitrile, pH 9.0, and mobile phase B is acetonitrile. The linear gradient is as follows: 0 minutes, 85% B; 1.5 minutes, 85% B, 5.5 minutes, 30% B; 8 minutes, 30% B, 10 minutes, 85% B, and 12 minutes, 85% B. The flow rate was 0.2 mL/minute. Sample volumes of 5 μL were injected for LC-MS analysis. LC-MS analysis was performed on a Q-exactive mass spectrometer (Thermo Fisher Scientific) equipped with a HESI probe, and the relevant parameters are as listed: heater temperature, $120°$C; sheath gas, 30; auxiliary gas, 10; sweep gas, 3; spray voltage, 2.5 kV for the negative mode. A full scan ranges from 80 to 350 (m/z) was used. The resolution was set at 70,000. Data were quantified by integrating the area underneath the curve of each compound using X calibur Qual browser (Thermo Fisher Scientific). Each metabolite's accurate mass ion and subsequent isotopic ions were extracted (EIC) using a 10-ppm window.

Real-time PCR

RNAs were extracted in TRIzol reagent (Invitrogen) and isolated according to the manufacturer's protocol and cDNAs were generated using the reverse transcription (ReverTra Ace qPCR Kit, Toyobo). Real-time PCR was performed for all genes using primers on the Bio-Rad CFX Connect and the data were captured using Bio-Rad CFX Manager 2.0 software. The mRNA expression of genes of interest was normalized to β-actin. The primer sequences are shown in Supplementary Methods.

Western blot analysis

Cell lysates preparation, SDS-PAGE, electrophoretic transfer, immunoblotting, and chemiluminescent detection were performed as described previously (5). Antibodies and dilutions are as follows: G6PD at 1:1,000 (Cell Signaling Technology, 12263S), PGD at 1:1,000 (Cell Signaling Technology, 13389S), HK2 at 1:1,000 (Cell Signaling Technology, 2867S), PCK1 at 1:1,000 (Cell Signaling Technology, 12940S), FBP1 at 1:1,000 (Abcam, ab109732), G6Pase at 1:500 (ab83690), β-actin at 1:1,000 (Cell Signaling Technology, 3700S), histone H3 at 1:1,000 (Cell Signaling Technology, 4499S), FoxO1 at 1:1,000 (Abcam, ab39670), PGM1 at 1:1,000 (Abcam, ab192876), PYGL at 1:1,000 (Abclonal, A6710), GDE at 1:1,000 (Proteintech, 16582), hypoxia-inducible factor 1α (HIF1α) at 1:1,000 (GeneTex, GTX127309).

Immunofluorescence staining

Animals were sacrificed and tumor tissues were isolated, fixed by 4% paraformaldehyde, embedded in paraffin and sectioned for immunofluorescence staining as described previously (5). Briefly, the sections

were prepared through dewaxing, antigen retrieval before staining. Then, sections were incubated with anti-ALDH1A1(1:200, Thermo Fisher Scientific), anti-pimonidazole (1:50, Hypoxyprobe), and anti-Ki67 (1:50, BioLegend) antibody at $4°$C overnight. Slides were then incubated sequentially with fluorescence-conjugated secondary antibodies for 1 hour at room temperature. DAPI was stained for nucleus and sections were observed under microscope (Leica TCS SP8 STED).

Generation of CRISPR-cas9 knockout cell lines

For construction of the stable knockdown of PCK1-MCF7 cells, the following SGRNAs targeting *PCK1* were used: *PCK1*-SGRNA1, forward 5′-CACCGAGGCCG TTTTGCAGCTGAGG-3′, reverse 5′-AAACCCTCAGCTGCAAAACGGCCTC-3′; *PCK1*-SGRNA2, forward 5′-CACC GCTCTCGGCCAAAGTTGTCCA-3′, reverse 5′-AAACTGGACAACTTTGGCCG AGAGC-3′. These SGRNAs were cloned into the pL-CRISPR.EFS.GFP vector plasmid and transfected HEK 293T cells together with the packing plasmids psPAX2 and pMD2G. Forty-eight hours later, the lentivirus was harvested and concentrated to infect MCF7 cells together with polybrene at a final concentration of 8 μg/mL. Two days later, GFP-positive cells were sorted by flow cytometry using the BD Biosciences FACS Aria III. The candidate knockout cells were verified by Western blot analysis.

ChIP-qPCR

A chromatin immunoprecipitation (ChIP) assay kit (Active Motif) was used to examine the binding of FoxO1 to the promoter of *PCK1*, the binding of HIF1α to the promoter of *PCK1*, or the binding of H3K27me3 and H3K4me3 to PCK1 as described previously (5). In brief, hypoxic and normoxic MCF7 bulk cells or TRCs were fixed with 1% formaldehyde on ice to crosslink the proteins bound to the chromatin DNA. After washing, the chromatin DNA was sheared by enzymatic force to produce DNA fragments of around 200 to 1,000 bp. The same amounts of sheared DNA were used for immunoprecipitation using anti-HIF1α, anti-FoxO1, anti-H3K4me3, and anti-H3H27me3 or an equal amount of preimmune rabbit IgG (GeneTex). The immunoprecipitate was then incubated with protein G Magnetic Beads, and the antibody–protein G magnetic beads complex was collected for subsequent reverse cross-linking. The same amount of sheared DNA without antibody precipitation was processed for reverse cross-linking and served as input control. DNA recovered from reverse cross-linking was used for qPCR. ChIP-qPCR primers are shown in Supplementary Methods.

Luciferase assays

Luciferase assays were performed according to our previously described methods (5). In brief, MCF7 cells were transfected with 100 ng *Renilla* luciferase, 1 μg firefly luciferase plasmid pGV238-PCK1 promoter-luc and 1 μg overexpressed plasmid of GV141-HIF1α or GV141-FoxO1 for 12 hours. Then, these cells were cultured for 36 hours. Cells lysates were analyzed using the Dual Luciferase Reporter Assay (Promega) on a GloMax Multi Plus (Promega). Firefly luciferase activity was normalized to *Renilla* luciferase. Similarly, MCF7 cells were transfected with 100 ng *Renilla* luciferase, 1 μg firefly luciferase plasmid pGV238-PCK1 promoter-luc, and siRNA of HIF1α or FoxO1 for 6 hours; after 48 hours, cells lysates were analyzed as above.

ROS detection

ROS levels were measured using CellROX Green Flow Cytometry Assay Kits (Life Technologies). Cells were loaded with 500 nmol/L CellROX Green for 30 minutes at $37°$C, protected from light. Cells

were washed and scraped in PBS and immediately analyzed by flow cytometry, using 488 nm excitation for the CellROX Green.

NADPH/NADP$^+$ and GSH/GSSG assay

The NADPH/NADP$^+$ ratio was determined using the NADP/NADPH Quantification Colorimetric Kit (BioVision KA1663, Abnova). Measurements were performed according to the manufacturer's instructions. The GSH/GSSG ratio was measured by LC-MS.

^{18}F-FDG PET/CT imaging

Before PET imaging, the mice were fasted for 12 hours and then approximately 200 $\pm$ 10 µCi 18-fluoro-6-deoxy-glucose (FDG) was injected by intravenous injection. After 60 minutes of FDG uptake, mice were anesthetized with 2% isoflurane and placed on scanning bed. PET/CT images were obtained with the static mode for 10 minutes, followed by CT scan of normal mode by the TransPET Discoverist 180 system (Raycan Technology Co., Ltd). The PET images were reconstructed using the three-dimensional (3D) OSEM method with a voxel size of $0.5 \times 0.5 \times 0.5$ mm^3. CT images were reconstructed using FDK algorithm with $1,024 \times 1,024 \times 1,024$ matrix. Images were displayed with software Carimas (Turku PET Center). The mean standardized uptake value (SUV) was calculated using the following formula: mean pixel value with the decay-corrected region-of-interest activity (µCi/kg)/[injected dose (µCi)/weight (kg)].

^{18}F-FMISO PET/CT imaging

Before PET imaging, the mice were anesthetized with 2% isoflurane and then approximately 200 $\pm$ 10 µCi 18F-fluoromisonidazole (FMISO) was injected by intraperitoneal injection. After 120 minutes of FMISO uptake, mice were anesthetized with 2% isoflurane and placed on scanning bed. PET/CT images were obtained with the static mode for 10 minutes followed by CT scan of normal mode by the TransPET Discoverist 180 system (Raycan Technology Co., Ltd). The PET images were reconstructed using the 3D OSEM method with a voxel size of $0.5 \times 0.5 \times 0.5$ mm^3. CT images were reconstructed using FDK algorithm with $1,024 \times 1,024 \times 1,024$ matrix. Images were displayed with software Carimas (Turku PET Center). The mean standardized uptake value (SUV) was calculated using the following formula: mean pixel value with the decay-corrected region-of-interest activity (µCi/kg)/[injected dose (µCi)/weight (kg)].

Statistical analysis

All experiments were performed at least three times and the mice were randomly divided into groups in all animal studies. To determine the colony size, at least 30 colonies from different field were measured. Results were expressed as mean $\pm$ SEM and analyzed by two-tailed unpaired Student t test, one-way ANOVA, Pearson correlation test, or log-rank survival analysis. In all tests, P values of <0.05 were considered statistically significant. The analysis was conducted using the GraphPad Prism 8.0 software.

Data availability

The authors declare that all the data supporting the findings of this study are available within the article and its Supplementary Files and from the corresponding author on reasonable request.

Results

Abundant glycogen is present in hypoxic breast TRCs

In this study, we initially analyzed several glycogenesis-related enzymes including phosphoglucomutase 1 (PGM1), UDP-glucose pyrophosphorylase 2 (UGP2), and glycogen synthase 1 (GYS1) in human breast tumor tissue samples by using the TCGA (https://tcga-data.nci.nih.gov/) database of RNA sequencing (RNA-seq). We found that these 3 enzymes had a strong correlation with a worsen prognosis, suggesting that glycogen levels might be associated with breast cancer progression (Supplementary Fig. S1A). Given that glycogen synthesis is elevated in hypoxic tumor microenvironments and breast TRCs are apt to reside in more hypoxic tumor microenvironments (5, 25, 26), we wondered whether breast TRCs had a distinctive glycogen metabolic mode. Previously, we have applied biomechanical principles to generate soft 3D fibrin gels with 90 Pa stiffness to culture highly tumorigenic TRCs, which are mechanically soft and represent stem-like tumor cells in tumors (21–23). We thus analyzed glycogen levels in TRCs from 3 human breast cancer cell lines (MCF7, T47D, and SUM159). We found that the TRCs consistently had higher levels of glycogen than the corresponding bulk cells under normoxia (21% O$_2$), and this gap could be further amplified by hypoxia (1% O$_2$), as evidenced by PAS staining and colorimetric assay (**Fig. 1A** and **B**). Similar results were also observed under transmission electron microscope (TEM; **Fig. 1C**). HIF1α is an important transcription factor to mark hypoxia (27), which was highly presented in the hypoxic TRCs (Supplementary Fig. S1B). Using the TCGA database of RNA-seq data, we found that PGM1, UGP2, and GYS1 were positively correlated with HIF1α expression in human breast tumor tissue samples (Supplementary Fig. S1C). To further validate these results *in vivo*, we inoculated MCF7 cells to nude mice and analyzed the aldehyde dehydrogenase 1 (ALDH1)–positive tumor cells in the tumors, considering that this subpopulation cells is representative of breast TRCs (28, 29). Indeed, the stemness genes (*Aldh1a1, Sox2, Oct3/4, CD133,* and *Klf4*) were found to be upregulated in the ALDH1$^+$/sunitinib group, compared with other groups (Supplementary Fig. S1D). The high expression of ALDH1 in hypoxic TRCs was also confirmed by immunofluorescence staining (Supplementary Fig. S1E). The PAS staining and TEM showed that a large amount of glycogen was present in ALDH1$^+$ TRCs but not in ALDH1$^-$ tumor cells, which was also confirmed by colorimetric assay (**Fig. 1D–F**). Moreover, the glycogen levels could be further increased in the TRCs (**Fig. 1D–F**), if the tumors entered a more hypoxic state by the treatment of mice with sunitinib (60 mg/kg/day). In addition to MCF7, similar results were also obtained from T47D breast tumors (**Fig. 1G–I**). Together, these results suggest that a large amount of glycogen is accumulated in hypoxic breast TRCs but not in the differentiated tumor cells.

Hypoxia triggers gluconeogenesis to glycogenesis in breast TRCs

Glycogen synthesis is initiated from the transition of G6P to G1P. Several pathways can be the source of G6P, including gluconeogenesis, glycogenolysis, and glycolysis. Deeming glycogenolysis-derived G6P for glycogenesis as futile recycling, we thus focused on the glycolysis. However, glycolysis seemed not to be the source of G6P, because ^{13}C-glucose tracing did not show an increased M+6 glycogen (Supplementary Fig. S2A). Also, hexokinase-2 (HK2), the enzyme that catalyzes the conversion of glucose to G6P, was not upregulated and even lower in hypoxic TRCs relative to the control bulk cells (Supplementary Fig. S2B). In line with this result, a decreased expression of glucose transporters was found in hypoxic TRCs compared with the hypoxic bulk cells (Supplementary Fig. S2C). Thus, hypoxic TRCs possibly used gluconeogenesis to produce G6P. Indeed, the first two rate-limiting enzymes in gluconeogenesis, cytoplasmic phosphoenolpyruvate carboxykinase 1 (PCK1) that converts oxaloacetate (OAA) to
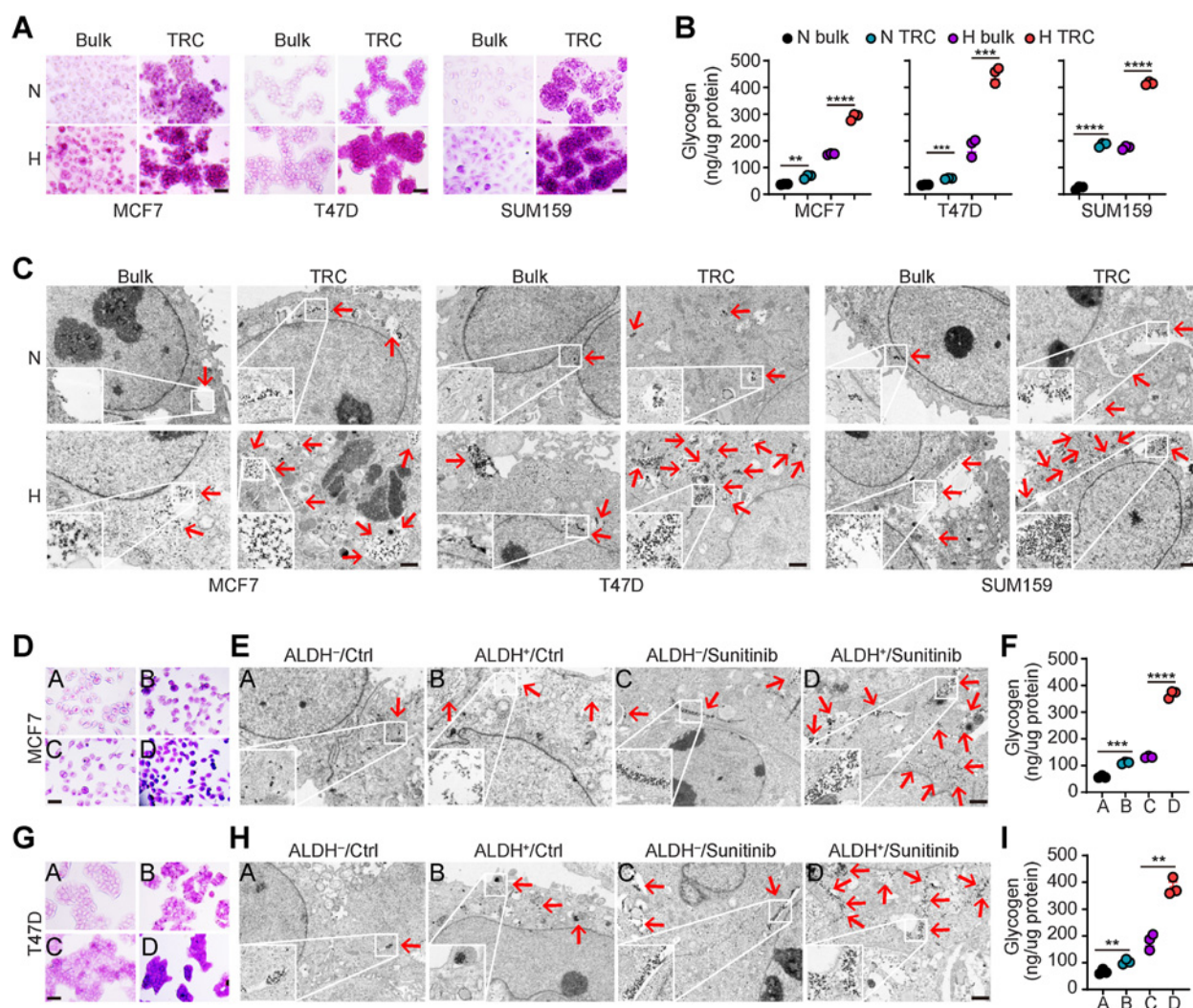
Figure 1.
Abundant glycogen is present in hypoxic breast TRCs. **A–C,** Glycogen levels in normoxic or hypoxic MCF7, T47D, or SUM159 cells cultured in rigid dish (bulk) or 90 Pa soft 3D fibrin gel (TRCs) for 5 days were detected by PAS staining (scale bar, 50 μmol/L; **A**), glycogen assay kit (**B**), and transmission electron microscopy (scale bar, 1 μm; **C**). Arrows, glycogen particles. **D–I,** MCF7 or T47D tumor cells (5×10^6) were inoculated into the mammary gland of nude mice, followed by intragastric administration of 60 mg/kg sunitinib per day. $n = 3$ mice per group. Thirty-five days later, mice were sacrificed, then ALDH1^{+} and ALDH1^{−} tumor cells were sorted from breast tumor tissue. Glycogen levels in MCF7 or T47D tumor were detected by PAS staining (scale bar, 50 μmol/L; **D** and **G**), transmission electron microscopy (scale bar, 1 μm; **E** and **H**), and glycogen assay kit (**F** and **I**). Arrows, glycogen particles. N, normoxia; H, hypoxia. Data are presented as mean ± SEM of $n = 3$ biologically independent experiments (**A–C**). P values were calculated using one-way ANOVA. **, $P < 0.01$; ***, $P < 0.001$; ****, $P < 0.0001$.

phosphoenolpyruvate (PEP) and fructose-1,6-bisphosphatase (FBP1) that converts fructose 1,6-bisphosphate to fructose 6-phosphate, were strikingly upregulated in hypoxic TRCs (MCF7, SUM159, and T47D), despite undetectable glucose-6-phosphatase (G6pase), the third rate-limiting enzyme that converts glucose-6-phosphate to glucose (**Fig. 2A** and **B**; Supplementary Fig. S2D). In addition, other breast cancer cell lines (HCC1937, HCC1806, ZR-75–1, and BT474) also upregulated the expression of PCK1 under hypoxia (Supplementary Fig. S2E; Supplementary Table S1). Using 3-MPA, a PCK1 inhibitor as well as *PCK1* siRNA (Supplementary Fig. S2F) to block gluconeogenesis, glycogen content was remarkably reduced in hypoxic TRCs (**Fig. 2C** and **D**), suggesting that the gluconeogenic pathway is used to guide glycogenesis in hypoxic TRCs. To further

verify this, we used ^{13}C-pyruvate, ^{13}C-acetate, or ^{13}C-glucose to treat hypoxic breast TRCs, which directly showed the transition of oxaloacetate (OAA) to M+2 PEP (**Fig. 2E**). Considering that OAA may come from glutamine, we also treated the cells with ^{13}C-glutamine. Consistent result was obtained as more M+3 PEP was produced under hypoxic TRCs (**Fig. 2F**). However, such M+2 or M+3 PEP production was reduced in hypoxic TRCs treated with 3-MPA or *PCK1* siRNA (**Fig. 2G** and **H**). In addition, we found that M+2 G6P/G1P (^{13}C-pyruvate or -acetate tracing) or M+3 G6P/ G1P (^{13}C-glutamine tracing) in hypoxic MCF7 TRCs was much higher than that in hypoxic bulk MCF7 cells (**Fig. 2I** and **J**). Together, these results suggest that hypoxic breast TRCs use the gluconeogenic pathway for glycogenesis.
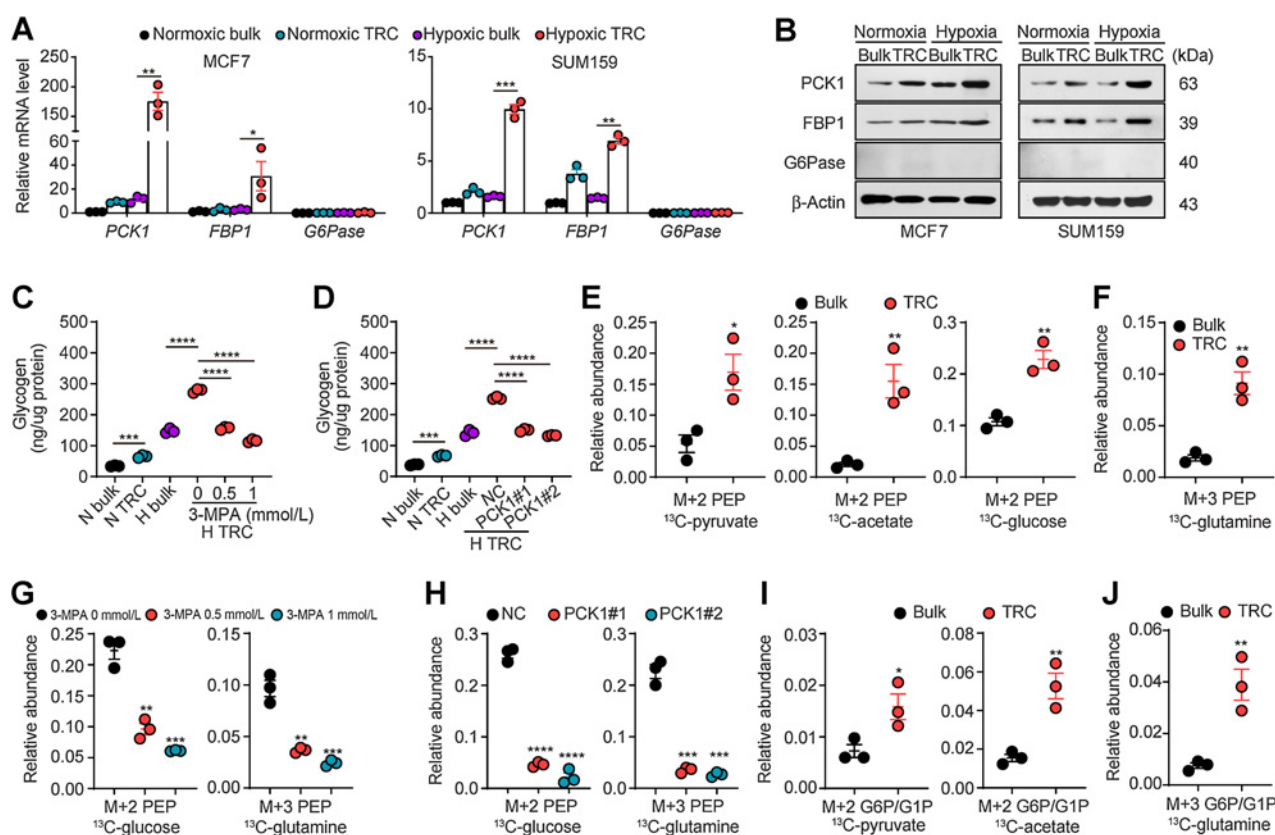
Figure 2.
Hypoxia triggers gluconeogenesis to glycogenesis in breast TRCs. **A** and **B,** The expression of PCK1, FBP1, and G6Pase in MCF7 or SUM159 bulk cells or TRCs under normoxia or hypoxia for 5 days was analyzed by real-time PCR (**A**) and Western blot analysis (**B**). **C** and **D,** Glycogen concentration in hypoxic MCF7 TRCs treated with 3-MPA or transfected with *PCK1* siRNA. **E** and **F,** MCF7 bulk cells or TRCs cultured under hypoxia were incubated with ^{13}C-pyruvate (**E**, left), ^{13}C-acetate (**E**, middle), ^{13}C-glucose (**E**, right), or ^{13}C-glutamine (**F**) for 24 hours, and LC-MS was performed for M+2- or M+3-labeled PEP, respectively. **G** and **H,** MCF7 TRCs treated with 3-MPA or transfected with *PCK1* siRNA under hypoxia were cultured with ^{13}C-glucose (left) or ^{13}C-glutamine (right) for 24 hours, and LC-MS was performed for M+2 or M+3 PEP, respectively. **I** and **J,** MCF7 bulk cells and TRCs cultured under hypoxia were incubated with ^{13}C-pyruvate (**I**, left), ^{13}C-acetate (**I**, right), or ^{13}C-glutamine (**J**) for 24 hours. The M+2 or M+3-labeled G6P/G1P was analyzed by LC-MS. G6P/G1P, total amount of G6P plus G1P. Data are presented as mean ± SEM of $n = 3$ biologically independent experiments. P values were calculated using one-way ANOVA (**C**, **D**, **G**, and **H**) and two-tailed unpaired Student t tests (**A**, **E**, **F**, **I**, and **J**). *, $P < 0.05$; **, $P < 0.01$; ***, $P < 0.001$; ****, $P < 0.0001$.

Hypoxia differentially regulates PCK1 in TRCs and bulk tumor cells

Next, we investigated how hypoxia regulates the key gluconeogenic enzyme PCK1. Upregulation of HIF1α is a universal cellular response to hypoxia. HIF1α has been shown to downregulate the expression of mitochondrial phosphoenolpyruvate carboxykinase (PCK2) in human cancer cells (5). Here, we unexpectedly found that HIF1α could upregulate PCK1 expression. Use of siRNA to knock down HIF1α (Supplementary Fig. S3A) led to the downregulation of PCK1 in hypoxic breast TRCs (**Fig. 3A**). In contrast, forced overexpression of HIF1α resulted in the upregulation of PCK1 in the TRCs (**Fig. 3B**). A ChIP-PCR assay showed that HIF1α was bound to the promoter of *PCK1* (**Fig. 3C**). In parallel, the luciferase reporter assay showed that HIF1α knockdown by siRNA decreased the luciferase activity and HIF1α overexpression increased the luciferase activity (**Fig. 3D**), suggesting that hypoxia can upregulate PCK1 expression in breast TRCs via HIF1α. In addition, FoxO1 is also known as an important transcription factor that regulates PCK1 expression (30, 31). As expected, both the ChIP-PCR and luciferase reporter assays showed that FoxO1 was bound to the *PCK1* promoter and regulated *PCK1*

positively (**Fig. 3E** and F). Moreover, FoxO1 was strikingly upregulated in hypoxic TRCs (**Fig. 3G**) and mainly located in the nucleus, consistent with its dephosphorylated active form (**Fig. 3H** and **I**). However, this FoxO1 upregulation could be disrupted by HIF1α knockdown (Supplementary Fig. S3B). Overexpression of FoxO1 led to the upregulation of PCK1 (**Fig. 3J**) and knockdown of FoxO1 (Supplementary Fig. S3A) resulted in the downregulation of PCK1 expression (**Fig. 3K**). Intriguingly, the pulldown assay showed that HIF1α did not associate with FoxO1 (**Fig. 3L**), suggesting that HIF1α and FoxO1 separately bind to the PCK1 promoter and together regulate PCK1 expression. Despite its upregulation in hypoxic TRCs, PCK1 expression in hypoxic bulk tumor cells is weak. While hypoxia similarly upregulated HIF1α in the bulk breast tumor cells, it had only a minor effect on FoxO1 expression and the nuclear translocation (**Fig. 3H** and **I**). By comparing the epigenetic modification between TRCs and bulk breast tumor cells, we found that there was no difference in the methylation status of the *PCK1* promoter region during normoxia and hypoxia (Supplementary Fig. S3C). However, a hypotrimethylation of H3K27 and a hypertrimethylation of H3K4 were observed in hypoxic TRCs (**Fig. 3M**) and PCK1 region was
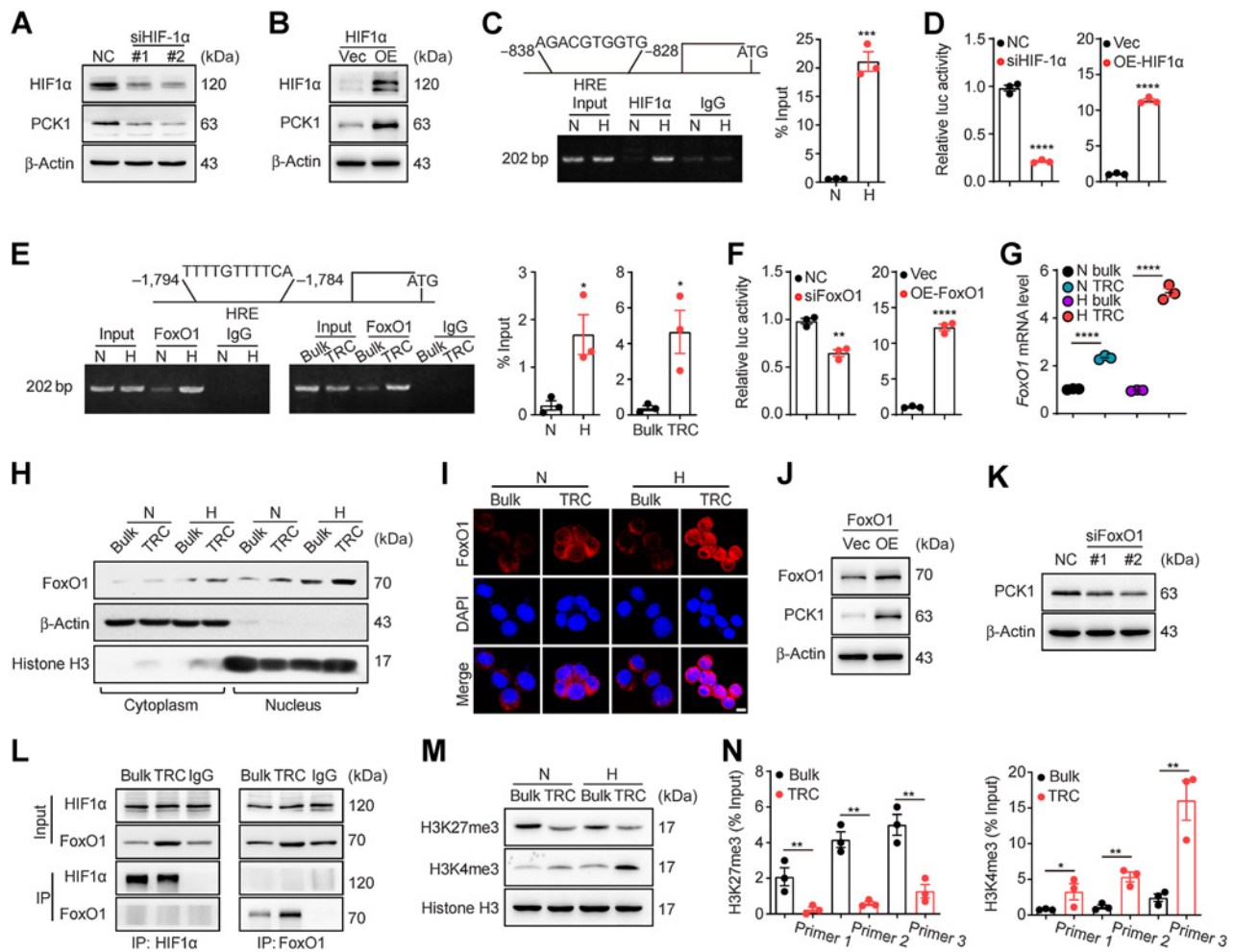
Figure 3.
Hypoxia differentially regulates PCK1 in TRCs and bulk tumor cells. **A** and **B,** MCF7 cells transfected with *HIF1α* siRNA (**A**) or overexpressing plasmid (**B**) were cultured in soft 3D fibrin gels in hypoxia or normoxia for 5 days; HIF1α and PCK1 expression was analyzed by Western blot analysis. **C,** Schematic representation of the promoter region, which was located at −838 to −828 bp on the upstream of the transcription start site of *PCK1*. MCF7 TRCs were cultured in 21% (N) or 1% (H) O$_2$ condition and then HIF1α enrichment around the promoter of *PCK1* were analyzed by ChIP-qPCR as described in Materials and Methods and IgG was used as a negative control. ChIP-qPCR was used for *PCK1* quantitative detection and total genomic DNA was used as input. **D,** MCF7 TRCs were transfected with *HIF1α* siRNA or overexpressing plasmid, and then the luciferase activity was detected as described in Materials and Methods. **E,** Schematic representation of the promoter region, which is located at −1,794 to −1,784 bp on the upstream of the transcription start site of *PCK1*. MCF7 bulk cells and TRCs were cultured in 21% (N) or 1% (H) O$_2$ condition and then FoxO1 enrichment around the promoter of *PCK1* was analyzed by ChIP-qPCR as described in Materials and Methods and IgG was used as a negative control. **F,** MCF7 TRCs were transfected with *FoxO1* siRNA or *FoxO1*-overexpressing plasmid, and then the luciferase activity was detected as described in Materials and Methods. **G–I,** MCF7 bulk cells or TRCs were cultured under normoxia and hypoxia for 5 days, and the expression of FoxO1 was analyzed using real-time PCR (**G**), Western blot analysis (**H**), and immunofluorescence (**I**). Scale bar, 10 μm. **J** and **K,** MCF7 cells transfected with *FoxO1* siRNA or overexpressing plasmid were cultured in soft 3D fibrin gels in hypoxia or normoxia for 5 days. FoxO1 and PCK1 expression was analyzed by Western blot analysis. **L,** Pulldown assay examining the interaction between HIF1α and FoxO1. Hypoxic bulk cell protein extracts were used in the IgG group and anti-IgG antibody was used as a negative control. **M** and **N,** MCF7 bulk cells or TRCs were cultured under normoxia and hypoxia for 5 days and then the methylation of histone H3K27 and H3K4 was analyzed by Western blot analysis (**M**) and the *PCK1* region was analyzed by ChIP-qPCR (**N**). N, normoxia; H, hypoxia. Data are presented as mean ± SEM of n = 3 biologically independent experiments. *P* values were calculated using one-way ANOVA (**G** and **N**) and two-tailed unpaired Student *t* tests (**C–F**). *, *P* < 0.05; **, *P* < 0.01; ***, *P* < 0.001; ****, *P* < 0.0001.

confirmed by ChIP-qPCR (**Fig. 3N**). Thus, in addition to FoxO1, this epigenetic reprogramming also explains why hypoxia can differentially regulate PCK1 in TRCs and the bulk tumor cells.

Hypoxia activates glycogenolysis-PPP in breast TRCs

Besides finding a high rate of glycogen synthesis, we also discovered that the glycogen underwent an active degradation process in hypoxic breast TRCs. Glycogen phosphorylase (PYGL), glycogen-debranching

enzyme (GDE), and phosphoglucomutase (PGM), three enzymes mediating glycogen breakdown, were upregulated in hypoxic breast TRCs (**Fig. 4A** and **B**; Supplementary Fig. S4A). Use of glycogen phosphorylase inhibitor GPI or the *PYGL* siRNA (Supplementary Fig. S4B) to block glycogenolysis could disrupt hypoxia-promoted breast TRC growth (**Fig. 4C** and **D**; Supplementary Fig. S4C and S4D), suggesting that the glycogenolysis is essential for hypoxic breast TRCs. G6P is the end product of glycogenolysis, which normally enters the
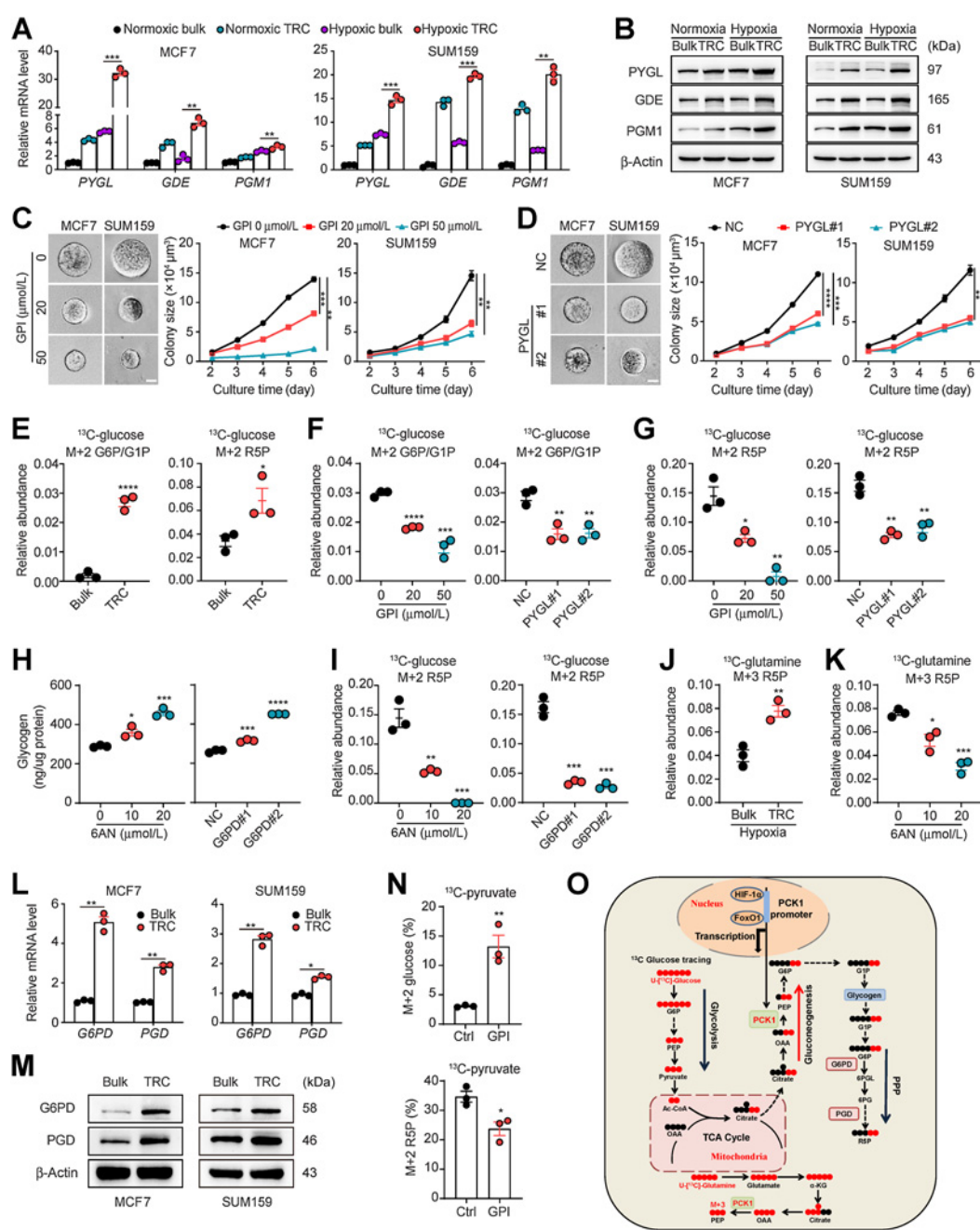
Figure 4.
Hypoxia activates glycogenolysis-PPP in breast TRCs. **A** and **B,** Expression of PYGL, GDE, and PGM1 in MCF7 and SUM159 bulk cells or TRCs under normoxia and hypoxia for 5 days was analyzed by real-time PCR and Western blot analysis. **C** and **D,** MCF7 or SUM159 cells were treated with GPI or transfected with *PYGL* siRNA and then cultured in soft 3D fibrin gels under hypoxia and colony size was analyzed. Scale bar, 20 μm. **E,** MCF7 bulk cells or TRCs cultured under hypoxia were incubated with ^{13}C-glucose for 24 hours, and LC-MS was performed for M+2 G6P/G1P or M+2 R5P, respectively. **F** and **G,** MCF7 TRCs cultured under hypoxia were treated with GPI or transfected with *PYGL* siRNA for 4 days, then incubated with ^{13}C-glucose for 24 hours, and M+2 G6P/G1P (**F**) or M+2 R5P (**G**) was analyzed by LC-MS. **H,** Glycogen concentration in MCF7 TRCs treated with 6AN or transfected with *G6PD* siRNA. **I,** MCF7 TRCs cultured under hypoxia were treated with 6AN or transfected with *G6PD* siRNA for 4 days, then incubated with ^{13}C-glucose for 24 hours, and M+2 R5P was analyzed by LC-MS. **J,** MCF7 bulk cells and TRCs cultured under hypoxia were cultured with ^{13}C-glutamine for 24 hours, and M+3 R5P was analyzed by LC-MS. **K,** MCF7 TRCs cultured under hypoxia were treated with 6AN for 4 days, then incubated with ^{13}C-glutamine for 24 hours and M+3 R5P was analyzed by LC-MS. **L** and **M,** PGD and G6PD expression in MCF7 and SUM159 bulk cells or TRCs under normoxia and hypoxia for 5 days was analyzed by real-time PCR and Western blot analysis. **N,** MCF7 TRCs cultured in ^{13}C-pyruvate medium in hypoxia were treated with GPI for 5 days. Cells in each setting were divided into two parts. One part was used for hydrochloric acid treatment and the ^{13}C-labeled monomer glucose was analysis. Another part was used for ^{13}C-labeled R5P detection by LC-MS. **O,** Schematic diagram for carbon tracing and signaling modulation in hypoxic breast TRCs. Data are presented as mean ± SEM of $n = 3$ biologically independent experiments. *P* values were calculated using one-way ANOVA (**C, D, F, G, H, I,** and **K**) and two-tailed unpaired Student *t* tests (**A, E, J, L,** and **N**). *, $P < 0.05$; **, $P < 0.01$; ***, $P < 0.001$; ****, $P < 0.0001$.

glycolytic pathway. However, the ^{13}C tracing assay showed that glycogenolysis-derived G6P/G1P was shunted to PPP by the detection of M+2 G6P/G1P and M+2 R5P (**Fig. 4E**), which could be blocked by GPI or *PYGL* siRNA (**Fig. 4F and G**). A consistent result was obtained from the ^{13}C-pyruvate tracing assay (Supplementary Fig. S4E and S4F). Blocking PPP by G6PD inhibitor 6-aminonicotinamide (6AN) or G6P dehydrogenase (*G6PD*) siRNA (Supplementary Fig. S4B) resulted in glycogen accumulation as well as a marked decrease of M+2 R5P in hypoxic breast TRCs (**Fig. 4H and I**). In addition to ^{13}C glucose, ^{13}C labeled glutamine tracing consistently showed that M+3 R5P was much higher in hypoxic TRCs compared with bulk tumor cells (**Fig. 4J**), which could be blocked by 6AN (**Fig. 4K**). In addition, we found that G6PD and 6-phosphogluconate dehydrogenase (PGD), two enzymes mediating the oxidative PPP, were upregulated in hypoxic TRCs (**Fig. 4L and M**; Supplementary Fig. S4G), suggesting that glycogenolysis-derived G6P may be channeled to PPP in hypoxic breast TRCs. To more clearly analyze the carbon flow of glycogenolysis-derived G6P, we used ^{13}C-pyruvate medium to culture breast TRCs for 5 days in 1% O$_2$ concentration. Glycogenolysis blockade by GPI led to the increase of ^{13}C-labeled M+2 glucose in glycogen from 3% to 13% and the decrease of M+2 R5P from 35% to 25% (**Fig. 4N**). The consistent percent alteration suggested that glycogenolysis derived G6P might flow to PPP in hypoxic TRCs. To better understand the above results, we additionally indicated the carbon flow of ^{13}C-glucose and ^{13}C-glutamine in hypoxic TRCs, as shown in **Fig. 4O**.

Glycogenolysis-PPP tunes ROS levels for hypoxic TRC growth

The carbon flow to PPP results in a direct production of NADPH, a key regulator of the antioxidative system. Previously, we had reported that hypoxic TRCs uses fumarate to succinate glutathione, thus decreasing ROS clearance (5). Here, we took this concept further by showing that hypoxic TRCs used glycogenolysis-PPP to regulate ROS levels. Thioredoxin and GSH are the two major antioxidative systems. Use of dinitrochlorobenzene (DNCB) to block the thioredoxin system only slightly increased ROS levels and had minor effect on hypoxic TRCs growth (**Fig. 5A**). In contrast, blocking GSH by buthionine (S, R)-sulfoximine (BSO) markedly increased ROS levels and inhibited hypoxic TRC growth (**Fig. 5B**). Mitochondria are the main sites where ROS is yielded. We found that BSO treatment indeed increased mitochondrial ROS in hypoxic TRCs (Supplementary Fig. S5A). PCK1-triggered gluconeogenesis yields intermediate metabolite 3-phosphoglycerate (3PG), which can be channeled to the serine metabolic pathway to generate glycine, an amino acid precursor necessary for GSH synthesis. Conducting the ^{13}C-pyruvate tracing, we found that the labeled ^{13}C was incorporated into the glutathione (Supplementary Fig. S5B), further suggesting that the GSH is involved in the regulation of ROS in hypoxic TRCs. In line with these results, hypoxia elevated the ratios of NADPH/NADP$^+$ and GSH/GSSG in breast TRCs (**Fig. 5C and D**; Supplementary Fig. S5C). However, such ratio elevation could be reversed by *G6PD* siRNA, concomitant with increased ROS levels (**Fig. 5E and F**) and decreased TRC growth (**Fig. 5G**; Supplementary Fig. S5D). A similar result was obtained by adding the G6PD inhibitor 6AN (Supplementary Fig. S5E–S5G). Of note, the effect of *G6PD* siRNA or 6AN could be counteracted by the addition of ethanol-GSH, the membrane permeable form of GSH (**Fig. 5H**; Supplementary Fig. S5H), suggesting that hypoxic breast TRCs use the PPP-dependent GSH system to tune ROS levels to promote their growth. Given the carbon flow from glycogenolysis to PPP, we also used *PYGL* siRNA or GPI to block glycogenolysis. Consistently, the NADPH/NADP$^+$ and GSH/GSSG ratios were decreased, concomitant with increased ROS levels (**Fig. 5I–K**; Sup-

plementary Fig. S5I and S5J). In addition, the use of *PCK1* siRNA or 3-MPA to block the gluconeogenesis produced similar results (**Fig. 5L–N**; Supplementary Fig. S5K–S5M). Meanwhile, the inhibitory effect of *PCK1* siRNA could be rescued by the GSH (Supplementary Fig. S5N). In parallel, the forced overexpression of PCK1 (Supplementary Fig. S5O) could increase colony size, NADPH/NADP$^+$ and GSH/GSSG ratios but decreased ROS levels in hypoxic TRCs (**Fig. 5O and P**). This increased colony size could be counteracted by BSO (Supplementary Fig. S5P). On the other hand, the use of *PYGL* siRNA to block glycogenolysis led to a decreased colony size, which however could be rescued by the addition of GSH (Supplementary Fig. S5Q). Together, these results suggest that the glycogenesis-glycogenolysis-PPP tunes ROS levels, allowing a moderately increased ROS level to favor hypoxic TRC growth.

Hypoxia triggers glycogen metabolic program in breast TRCs *in vivo*

Next, we validated the above *in vitro* data *in vivo*. We treated nude mice bearing palpable MCF7 tumor (50–100 mm^3) with sunitinib (60 mg/kg/day) for 35 days. We found that ALDH1$^+$ TRCs (28, 29) isolated from the hypoxic tumors highly expressed enzymes involved in gluconeogenesis, glycogen metabolism, and PPP, including *PCK1, FBP1, UGP2, GYS1, PYGL, G6PD*, and *PGD* (**Fig. 6A**). This result was not caused by the direct effect of sunitinib, because sunitinib did not affect PCK1 expression and glycogen levels in hypoxic TRCs *in vitro* (Supplementary Fig. S6A and S6B). In contrast to ALDH1$^+$ TRCs, these enzymes were extremely lowly expressed in the ALDH$^-$ cells (**Fig. 6A**). These sunitinib-treated ALDH$^+$ TRCs had much higher NADPH/NADP$^+$ and GSH/GSSG ratios than sunitinib-treated ALDH$^-$ cells (**Fig. 6B**). Also, these sunitinib-treated TRCs were in a proliferating state with high expression of Ki67 (Fig. 6C). Consistently, HIF1α knockdown resulted in the downregulation of ALDH1 expression in hypoxic MCF7 TRCs (Supplementary Fig. S6C). In addition, LC-MS analysis showed a higher carbon flow from gluconeogenesis to glycogen and ultimately to PPP in sunitinib-treated TRCs (**Fig. 6D**). Moreover, we inoculated nude mice with SGGFP- or *PCK1*-SGs-MCF7 cells into the mammary gland, followed by sunitinib treatment. We found that PCK1 knockdown retarded the tumor growth (**Fig. 6E and F**) and decreased NADPH/NADP$^+$ and GSH/GSSG ratios (**Fig. 6G**) but increased ROS levels in ALDH1$^+$ TRCs (**Fig. 6H**). On the other hand, inoculation of PCK1-overexpressing MCF7 cells to nude mice accelerated tumor growth, and led to increased NADPH/NADP$^+$ and GSH/GSSG ratios but decreased ROS levels (**Fig. 6I–K**). However, such effects were abrogated by the 3-MPA treatment (**Fig. 6L–N**). Here, we also analyzed 54 clinical breast cancer samples by immunohistochemical staining. We found that PCK1 expression was elevated in high stage tumors (**Fig. 6O**), correlating with an active tumor cell proliferation (**Fig. 6P**), and predicted a worse prognosis (**Fig. 6Q**). Together, these results suggest that hypoxia-induced PCK1 triggers a retrograde carbon flow from gluconeogenesis, glycogen to PPP, resulting in a tuned ROS level to promote hypoxic TRC growth in breast tumor.

Targeting PCK1-directed glycogen metabolism enhances TNBC treatment

The above elucidation of hypoxia-triggered glycogen metabolic program in highly tumorigenic breast TRCs provided a potential strategy to tackle triple-negative breast cancer (TNBC), a subtype of breast cancer with extreme resistance to conventional treatment. In fact, a severe hypoxia has been observed in xenograft TNBC models (32). By comparing different human breast tumor mouse models,
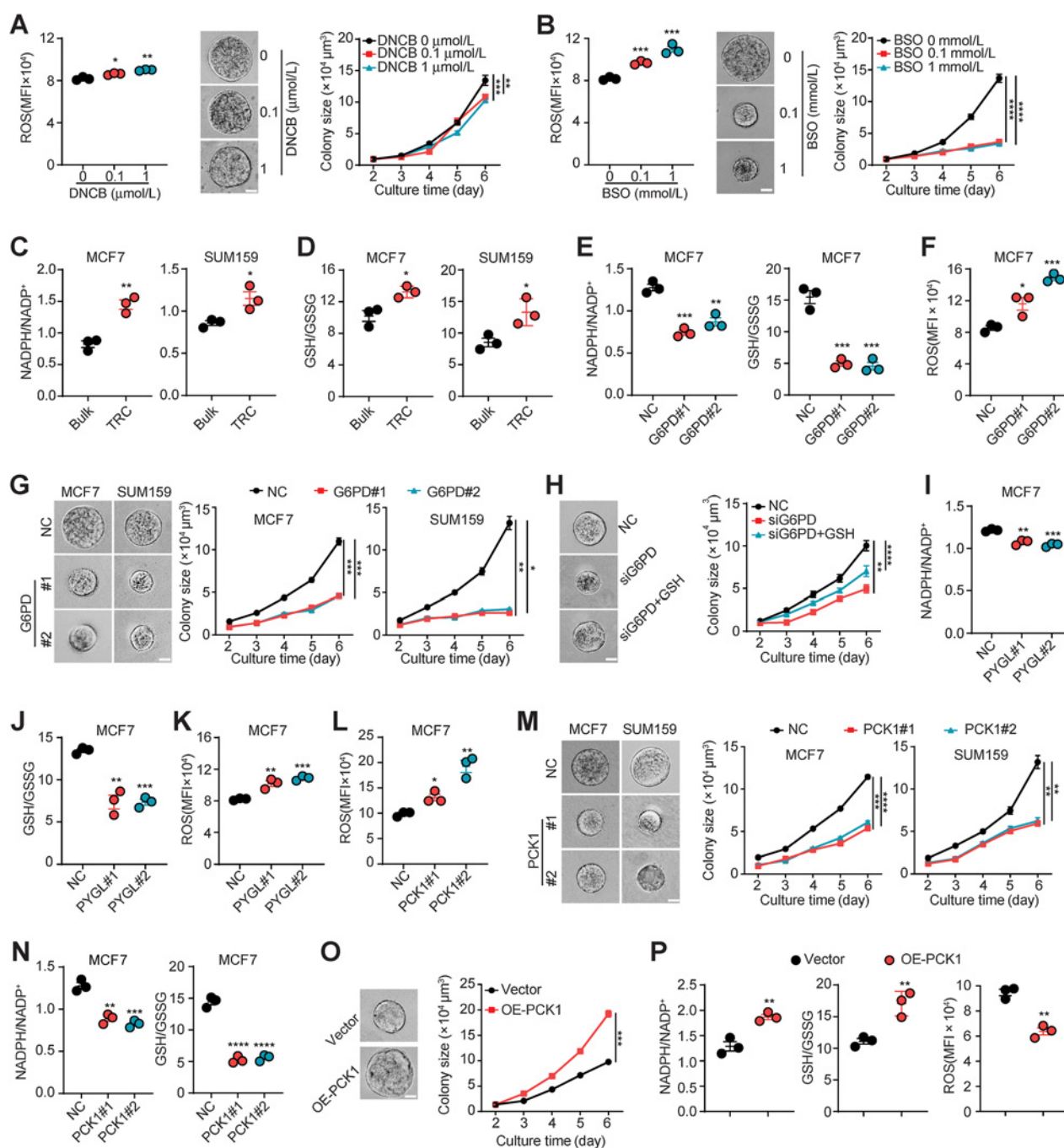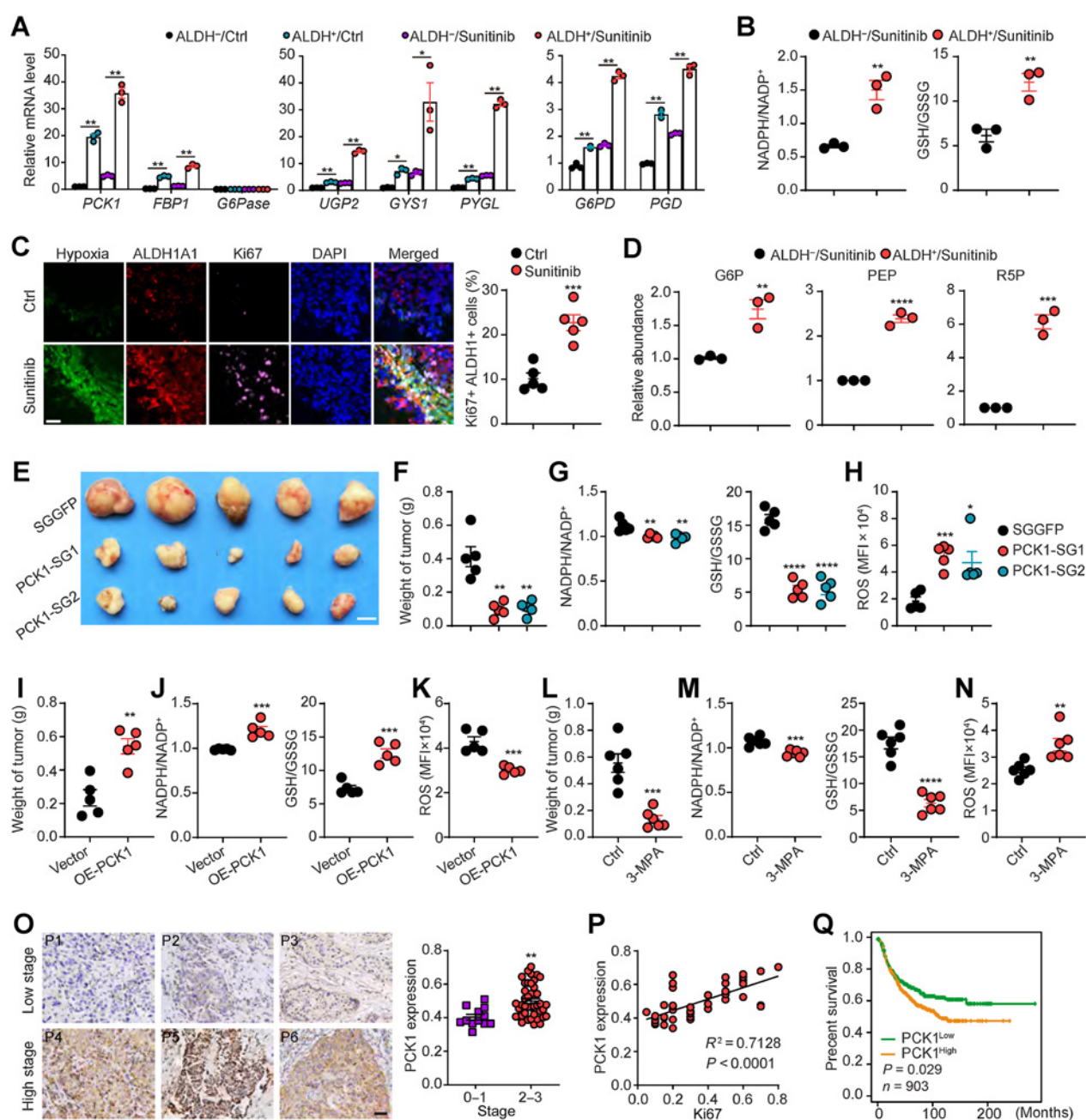
Figure 5.
Glycogenolysis-PPP tunes ROS levels for hypoxic TRC growth. **A** and **B,** ROS levels and the colony size were analyzed in hypoxic TRCs treated with DNCB (**A**) or BSO (**B**) for 6 days. Scale bar, 20 μm. **C** and **D,** NADPH/NADP$^+$ ratio (**C**) and GSH/GSSG levels (**D**) in MCF7 and SUM159 bulk cells or TRCs under hypoxia for 6 days. **E–G,** MCF7 or SUM159 cells were transfected with *G6PD* siRNA and then cultured in soft 3D fibrin gels under hypoxic condition (1% O$_2$). NADPH/NADP$^+$, GSH/GSSG ratio (**E**), ROS levels (**F**), and the colony size (**G**) were analyzed. Scale bar, 20 μm. **H,** MCF7 cells were transfected with *G6PD* siRNA and ethyl-GSH (2 mmol/L) for 6 days in hypoxia, and the colony size was analyzed. Scale bar, 20 μm. **I–K,** MCF7 cells were transfected with *PYGL* siRNA and then cultured in soft 3D fibrin gels under hypoxia. NADPH/NADP$^+$ ratio (**I**), GSH/GSSG ratio (**J**), and ROS levels (**K**) were analyzed. **L–N,** MCF7 or SUM159 cells were transfected with *PCK1* siRNA and then cultured in soft 3D fibrin gels under hypoxia. ROS levels (**L**), the colony size (**M**), NADPH/NADP$^+$ ratio, and GSH/GSSG ratio (**N**) were analyzed. Scale bar, 20 μm. **O** and **P,** MCF7 cells transfected with *PCK1*-overexpressing plasmid were cultured in soft 3D fibrin gels in hypoxia for 6 days, then colony size, NADPH/NADP$^+$ ratio, GSH/GSSG ratio, and ROS levels were analyzed. Scale bar, 20 μm. Data are presented as mean ± SEM of $n = 3$ biologically independent experiments. P values were calculated using one-way ANOVA (**A**, **B**, **E**, **F**, **G**, **H**, **I**, **J**, **K**, **L**, **M**, and **N**) and two-tailed unpaired Student t tests (**C**, **D**, **O**, and **P**). *, $P < 0.05$; **, $P < 0.01$; ***, $P < 0.001$; ****, $P < 0.0001$.

Figure 6.
Hypoxia triggers glycogen metabolic program in breast TRCs *in vivo*. **A–D,** MCF7 tumor cells (5×10^6) were inoculated into the mammary gland of nude mice, followed by intragastric administration of 60 mg/kg sunitinib per day. $n = 3$ mice per group. Thirty-five days later, mice were sacrificed and then ALDH1^{high} and ALDH1^{low} tumor cells were sorted from breast tumor tissue. The expression of *PCK1, FBP1, G6Pase, UGP2, GYS1, PYGL, G6PD*, and *PGD* (**A**) and NADPH/NADP$^+$, GSH/GSSG ratios (**B**) in MCF7 tumor were detected. Tumor tissues were stained as described in Materials and Methods and immunofluorescence staining showed pimonidazole (green), ALDH1 (red), and Ki67 (pink) merged with DAPI-stained nucleus (blue; **C**). Gluconeogenesis, glycogen metabolism, and PPP intermediates were detected by LC-MS (**D**). **E–K,** *PCK1*-SGs- (**E–H**) or *PCK1*-overexpressing (**I–K**) MCF7 TRCs were inoculated into mammary gland of nude mice and mice were treated with sunitinib as described in Materials and Methods. $n = 5$ mice per group. Thirty-five days later, mice were sacrificed and tumor mass was measured (scale bar, 0.5 cm; **E**, **F**, and **I**). The NADPH/NADP$^+$ ratios were analyzed as described in Materials and Methods (**G** and **J**). The GSH/GSSG ratios were detected by LC-MS (**G** and **J**). ROS levels were detected by flow cytometry (**H** and **K**). **L–N,** MCF7 TRCs were inoculated into mammary gland of nude mice and mice were administered intragastrically with sunitinib (60 mg/kg) combined with 3-MPA (30 mg/kg) or saline once per day. $n = 6$ mice per group. Thirty-five days later, mice were sacrificed and tumor mass was measured (**L**). The NADPH/NADP$^+$ ratios (**M**, left), GSH/GSSG ratios (**M**, right), and ROS levels (**N**) were detected. **O** and **P,** PCK1 expression in 54 patients with breast cancer at different stages and correlation between PCK1 and Ki67. Scale bar, 50 μm. **Q,** Overall survival compared with the PCK1 level in patients with breast cancer (BRCA; $n = 903$); data were analyzed with the Kaplan–Meier plotter (http://kmplot.com/analysis/). P values were calculated using one-way ANOVA (**A**, **F**, **G**, and **H**), two-tailed unpaired Student t tests (**B**, **C**, **D**, **I**, **J**, **K**, **L**, **M**, **N**, and **O**), Pearson correlation test (**P**), and log-rank survival analysis (**Q**). *, $P < 0.05$; **, $P < 0.01$; ***, $P < 0.001$; ****, $P < 0.0001$.
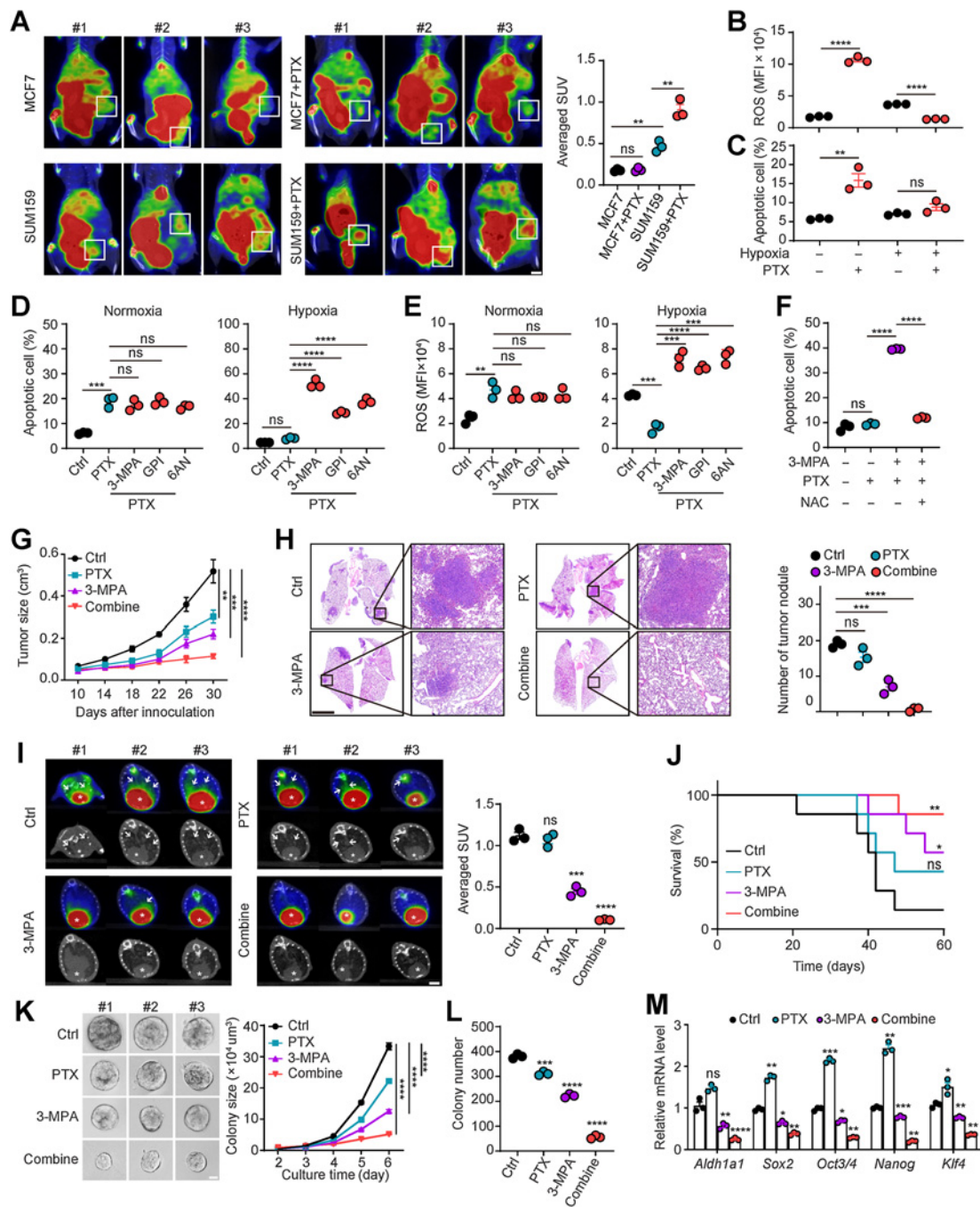
Figure 7.
Targeting PCK1-directed glycogen metabolism enhances TNBC treatment. **A,** MCF7 and SUM159 tumors were imaged using PET/CT with ¹⁸F-FMISO on day 21 after paclitaxel (PTX) treatment. The tumors are indicated by squares. $n = 3$ mice per group. Scale bar, 5 mm. **B** and **C,** SUM159 TRCs were treated with 5 μg/mL paclitaxel for 36 hours under normoxia and hypoxia. ROS levels (**B**) and cell viability (**C**) were analyzed by flow cytometry. **D** and **E,** SUM159 TRCs were treated with 5 μg/mL paclitaxel alone or in combination with 3-MPA, GPI, or 6AN under normoxia and hypoxia. Cell apoptosis (**D**) and ROS levels (**E**) were analyzed by flow cytometry. **F,** SUM159 TRCs were treated with 1 μg/mL paclitaxel alone or in combination with 3-MPA and NAC under hypoxia. Cell apoptosis was analyzed by flow cytometry. **G–M,** SUM159 TRCs cells (1 × 10⁶) were inoculated into the mammary gland of nude mice. Then, mice were intraperitoneally injected with 10 mg/kg paclitaxel (once per week), or intragastric administered 30 mg/kg 3-MPA or saline control for 4 weeks. Tumor growth (**G**) was monitored. Then, mice were sacrificed and the lung metastasis was analyzed by hematoxylin and eosin staining (scale bar, 0.5 mm; **H**) and PET-CT (scale bar, 5 mm; **I**). The arrows show the tumor on the lung region in transversal sections and the asterisks show the heart. The survival of mice (**J**) was monitored. Cells isolated from tumor were reseeded into soft 3D fibrin gels in hypoxia for 6 days, and the colony size (**K**) and the number of TRCs (**L**) were analyzed. Scale bar, 20 μm. *Aldha1, Sox2, Oct3/4, Nanog,* and *Klf4* mRNA levels were analyzed by real-time PCR (**M**). SUV, standardized uptake value. Data, mean ± SEM. *P* values were calculated using one-way ANOVA (**A**, **D**, **E**, **F**, **G**, **H**, **I**, **K**, **L**, and **M**), two-tailed unpaired Student *t* tests (**B** and **C**), and two-sided log-rank (Mantel–Cox) test (**J**). *, $P < 0.05$; **, $P < 0.01$; ***, $P < 0.001$; ****, $P < 0.0001$; ns, no significance.

we found that SUM159 TNBC tumors were also more hypoxic than MCF7 tumors (**Fig. 7A**). Surprisingly, treatment with paclitaxel, the first-line drug for TNBC, aggravated the hypoxia in TNBC tumors but not in MCF7 tumors (**Fig. 7A**). In line with this hypoxia, endothelial damage caused by paclitaxel was overt in TNBC tumors (Supplementary Fig. S7A). Meanwhile, carbonic anhydrase IX (CA9), an indicator of hypoxia (33), was upregulated in TNBC tumors (Supplementary Fig. S7B) and this was verified using the TCGA (https://tcga-data.nci.nih.gov/) database of RNA-seq (Supplementary Fig. S7C). Moreover, PCK1 expression was enhanced in hypoxic areas compared with normoxic areas (Supplementary Fig. S7D). We found that the *in vitro* 5 μg/mL paclitaxel treatment decreased ROS levels of hypoxic SUM159 TRCs but did not cause the cell death (**Fig. 7B** and **C**), which however was induced by the combination of 3-MPA, GPI, or 6AN, concomitant with elevated ROS levels (**Fig. 7D** and **E**). Notably, even low-dose paclitaxel (1 μg/mL) could kill the TRCs effectively in the combination with 3-MPA and such killing could be rescued by ROS scavenger NAC (**Fig. 7F**). For this *in vitro* experiment, we additionally tested MCF7, T47D, and another two TNBC cells (HCC1937 and HCC1806) and the similar result was obtained (Supplementary Fig. S7E and S7F). In addition to paclitaxel, we also tested cisplatin and found that the combination of cisplatin and 3-MPA also generated an enhanced treatment outcome (Supplementary Fig. S7G). Then, we treated SUM159 cell-inoculated mice with 3-MPA and paclitaxel. We found that although paclitaxel alone had marginal treatment effect, the combined treatment strongly inhibited tumor growth, reduced tumor metastasis and prolonged the long-term survival of the mice (**Fig. 7G–J**). In addition, this combination did not show overt side effect (Supplementary Fig. S7H). We also seeded bulk tumor cells isolated in the 90 Pa soft 3D fibrin gels, a biomechanical method that selects and amplifies TRCs, to monitor the alteration of tumorigenic cells after treatment. We found that the colony size and the number in the gels were reduced in the combined treatment group (**Fig. 7K** and **L**). In addition, 3-MPA treatment downregulated stemness gene expression (*Aldh1a1, Sox2, Oct3/4, Nanog*, and *Klf4*), which could be further downregulated by the combined treatment (**Fig. 7M**). Together, these results suggest that targeting PCK1-directed glycogen metabolic program potentially enhances paclitaxel treatment of TNBC.

Discussion

Tumor cells synthesize glycogen in response to surrounding hypoxia (11–13). However, the biological significance of such glycogen in hypoxic tumor cells remains elusive. In this study, we provide evidence that highly tumorigenic human breast TRCs use hypoxia-responsive transcription factor HIF1α to upregulate PCK1, thus triggering the carbon flow along a metabolic chain of gluconeogenesis-glycogenesis-glycogenolysis-PPP, tuning ROS levels via the NADPH-glutathione system, and subsequently promoting TRC growth. Unveiling this reprogrammed metabolic way may explain how tumorigenic cells adapt to a hypoxic microenvironment, leading to enhanced tumor metastasis and malignancy.

Stiffness is an inherent feature of a cell, which is mainly provided by F-actin filaments. Different cell types display varying levels of stiffness, which matches the stiffness of the local extracellular matrix, allowing the cells to properly sense and respond to the surrounding mechanical microenvironments (34, 35). Based on this understanding, we have developed a mechanics-based culture system using 3D soft fibrin gels that can selectively amplify TRCs from primary tumor tissues and cancer cell lines in both murine and human settings (18, 21, 22, 36–38).

We have demonstrated that breast cancer TRCs including MCF7 TRCs are very soft and highly express stemness markers (18, 23). Also, these TRCs are highly tumorigenic. As few as 10 TRCs, after intravenous injection via the tail vein, are able to grow tumors in the lungs of immunocompetent mice (21). Or, 5 TRCs grow a tumor in the skin of wild-type mice (39). Although TRCs are initially identified *in vitro* using the 90 Pa 3D fibrin gels, this subpopulation of tumor cells has recently been demonstrated *in vivo*, which actually belong to a group of soft tumor cells in contrast to most tumor cells that are stiff in the whole tumor cell population (28). Considering our findings and previous reports on the positive association between increased tissue stiffness and aggressive cancer behaviors like proliferation and metastasis (40, 41), it is likely that stiff matrix has the promoting effect on the differentiated stiff tumor cells but not on undifferentiated soft tumor cells. In addition, TRCs are distinct from the conventional cancer stem cells (CSC) that are isolated by using unreliable cell surface markers (42). In fact, CSCs contain both soft and stiff tumor cells, and only the soft cells but not the stiff ones are able to grow a tumor (28). Biologically, the softness endows TRCs with deformability, thus facilitating metastasis. This softness can also mediate the escape of CD8+ T-cell killing by impairing membrane perforin pore formation (43). However, such softness can be utilized by tumor microparticles to deliver chemotherapeutic drug into the nucleus, thus causing TRC death (38). In the current study, we further demonstrate that breast TRCs are benefitted by hypoxia. They tactfully launch an altered glycogen metabolic program in response to hypoxic stress, acquiring an increased ability to proliferate. Taken together, the finding of hypoxia-promoted breast TRC growth is of paramount importance considering that TRCs are the root cause of tumor recurrence, metastasis, and drug resistance.

Cells use the TCA cycle and OXPHOS to generate ATP for life. In this metabolic mode, glucose oxidation–generated reducing equivalents NADH and FADH2 enter the mitochondrial electron transport chain (ETC), where NADH and FADH2 become NAD+ and FAD, respectively, and release electrons and energy. The electrons are then transferred along the ETC, while the released energy pumps proton from the matrix to the intermembrane space to form a proton gradient. When electrons are transferred to complex IV, the protons across the inner membrane back to the matrix where molecular oxygen, protons, and electrons react to produce H_2O and the corresponding chemiosmotic power is captured by the membrane-spanning enzyme ATP synthase, thus catalyzing the addition of a phosphate to ADP (44–46). This ATP-forming process sounds perfect; however, the imperfection is that electrons may leak from the ETC and react with molecular oxygen without proton to generate superoxide anion, the prototype of ROS, which may cause damage to the cells (46, 47). It is originally believed that hypoxia-decreased O_2 supply to the mitochondria can reduce superoxide anion production, thus favoring a decrease in ROS content. However, accumulating evidence is showing that ROS is increased in hypoxic tumor cells (5, 48, 49). The NADPH oxidase system may be a source of increased $O_2^{\bullet-}$ in response to hypoxia; however, mitochondria-derived ROS is considered the major reason (50–52). Under hypoxic stress, tumor cells need to develop strategies to combat ROS attack.

Despite the conventional notion that G6P from glycogen breakdown is directly oxidized along the glycolysis (12, 53), in this study, we found that hypoxia drives the shunt of glycogenolysis-derived G6P to the PPP and the carbon returns to the glycolysis in the form of fructose-6-phosphate and glyceraldehyde-3-phosphate in highly tumorigenic human breast TRCs. This unusual metabolic way not only generates ATP but also mobilizes the NADPH machinery to quench ROS.

Cancer has been described as an atavism and the tumorigenic cells might be more like the original primitive cells who live in an anaerobic environment and only use glycolysis to generate ATP (54, 55). From an evolutionary perspective, the glycogen-PPP-glycolysis metabolic mode might not be surprising, merely announcing that TRCs have a versatile adaption to hypoxia. However, considering that OXPHOS is much more efficient in ATP production than glycolysis and that ROS can be quenched by the reprogrammed glycogen-PPP metabolic way, TRCs seem to surpass the ancient cells, which only use glycolysis to generate ATP. Undoubtedly, enough energy supplement drives cell growth. In our previous study, we indeed found that a moderately increased ROS activates Akt and NF-κB, thus promoting hypoxic human breast TRC growth (5). But, how the Akt and NF-κB signaling in turn regulate the reprogrammed glycogen-PPP metabolic way is unclear and worthy of further investigation.

Cell growth and proliferation are regulated by various signal molecules, which reprogram cellular metabolism to fulfill the biosynthetic needs for cell growth and division. In this study, we demonstrate that HIF1α regulates PCK1 expression, thus triggering a gluconeogenesis-glycogenesis-glycogenolysis-PPP metabolic chain. Therefore, HIF1α activation is a very important event in the metabolic adaptation of hypoxia. HIF1α degradation by von Hippel–Lindau ubiquitin E3 ligase complex requires prolyl hydroxylation of HIF1α. This reaction by prolyl hydroxylase PHD needs O_2 as a substrate, thus allowing hypoxia to mediate the stabilization of HIF1α (27, 56, 57). Besides, during hypoxia, fumarate is accumulated in the TRCs through the reprogrammed TCA cycle, further stabilizing HIF1α, because succinate is able to compete with αKG for PHD binding (58). In addition, ROS-activated Akt may enhance translation of HIF1α mRNA through mTORC1 (59, 60). Thus, overexpression of HIF1α is guaranteed through multiple mechanisms in hypoxic human breast TRCs. In addition to gluconeogenesis-related PCK1, the upregulation of genes involved in glycogenesis, glycogenolysis, and PPP are also found in this study. Whether HIF1α is also involved in the regulation these genes is not investigated in the present study. How these corresponding enzymes are tuned to incorporate into the above metabolic chain for TRCs adapting hypoxia needs to be elucidated in the future study.

In summary, our data show that human breast cancer TRCs, by virtue of their upregulating the key gluconeogenic enzyme PCK1 that reprograms a gluconeogenesis-glycogenesis-glycogenolysis-PPP metabolic chain, are admirably adapted to hypoxia and grow rapidly in hypoxic conditions. The G6P from PCK1-driven gluconeogenesis is channeled to glycogenesis and glycogenolysis successively, and the regenerated G6P however fluxes to the PPP, thus leading to NADPH production and subsequent ROS reduction by the GSH system in hypoxic breast TRCs. These findings provide deeper insights into how highly tumorigenic cells reprogram their metabolism in response to hypoxia. Thus, targeting this unusual metabolic way is highlighted to generate a better tumor treatment efficiency, as evidenced in the TNBC treatment in this study.

Authors' Disclosures

No disclosures were reported.

Authors' Contributions

K. Tang: Resources, data curation, funding acquisition, investigation, methodology, writing–original draft, project administration, writing–review and editing. **L. Zhu:** Data curation, software, formal analysis. **J. Chen:** Data curation. **D. Wang:** Data curation, software. **L. Zeng:** Data curation, software. **C. Chen:** Data curation. **L. Tang:** Data curation. **L. Zhou:** Data curation. **K. Wei:** Data curation. **Y. Zhou:** Software, methodology. **J. Lv:** Data curation. **Y. Liu:** Data curation. **H. Zhang:** Data curation, software, supervision. **J. Ma:** Data curation, software, supervision. **B. Huang:** Conceptualization, supervision, funding acquisition, writing–original draft, project administration, writing–review and editing.

References

1. Bertout JA, Patel SA, Simon MC. The impact of O2 availability on human cancer. Nat Rev Cancer 2008;8:967–75.
2. Vaupel P, Höckel M, Mayer A. Detection and characterization of tumor hypoxia using pO2 histography. Antioxid Redox Signal 2007;9:1221–35.
3. Jing X, Yang F, Shao C, Wei K, Xie M, Shen H, et al. Role of hypoxia in cancer therapy by regulating the tumor microenvironment. Mol Cancer 2019;18:157.
4. You L, Wu W, Wang X, Fang L, Adam V, Nepovimova E, et al. The role of hypoxia-inducible factor 1 in tumor immune evasion. Med Res Rev 2021;41:1622–43.
5. Tang K, Yu Y, Zhu L, Xu P, Chen J, Ma J, et al. Hypoxia-reprogrammed tricarboxylic acid cycle promotes the growth of human breast tumorigenic cells. Oncogene 2019;38:6970–84.
6. Rezaeian AH, Li CF, Wu CY, Zhang X, Delacerda J, You MJ, et al. A hypoxia-responsive TRAF6-ATM-H2AX signalling axis promotes HIF1α activation, tumorigenesis and metastasis. Nat Cell Biol 2017;19:38–51.
7. de Heer EC, Jalving M, Harris AL. HIFs, angiogenesis, and metabolism: elusive enemies in breast cancer. J Clin Invest 2020;130:5074–87.
8. Nicholas DC. Hypoxia, HIF1 and glucose metabolism in the solid tumour. Nat Rev Cancer 2008;8:705–13.
9. Chen C, Pore N, Behrooz A, Ismail-Beigi F, Maity A. Regulation of glut1 mRNA by hypoxia-inducible factor-1. Interaction between H-ras and hypoxia. J Biol Chem 2001;276:9519–25.
10. Conley SJ, Gheordunescu E, Kakarala P, Newman B, Korkaya H, Heath AN, et al. Antiangiogenic agents increase breast cancer stem cells via the generation of tumor hypoxia. Proc Natl Acad Sci U S A 2012;109:2784–9.
11. Pelletier J, Bellot G, Gounon P, Lacas-Gervais S, Pouysségur J, Mazure NM. Glycogen synthesis is induced in hypoxia by the hypoxia-inducible factor and promotes cancer cell survival. Front Oncol 2012;2:18.
12. Dauer P, Lengyel E. New roles for glycogen in tumor progression. Trends Cancer 2019;5:396–9.
13. Zhang H, Ma J, Tang K, Huang B. Beyond energy storage: roles of glycogen metabolism in health and disease. FEBS J 2021;288:3772–83.
14. Ma J, Wei K, Liu J, Tang K, Zhang H, Zhu L, et al. Glycogen metabolism regulates macrophage-mediated acute inflammatory responses. Nat Commun 2020;11:1769.
15. Owczarek A, Gieczewska K, Jarzyna R, Jagielski AK, Kiersztan A, Gruza A, et al. Hypoxia increases the rate of renal gluconeogenesis via hypoxia-inducible factor-1-dependent activation of phosphoenolpyruvate carboxykinase expression. Biochimie 2020;171–172:31–37.
16. Choi JH, Park MJ, Kim KW, Choi YH, Park SH, An WG, et al. Molecular mechanism of hypoxia-mediated hepatic gluconeogenesis by transcriptional regulation. FEBS Lett 2005;579:2795–801.
17. Ma R, Zhang W, Tang K, Zhang H, Zhang Y, Li D, et al. Switch of glycolysis to gluconeogenesis by dexamethasone for treatment of hepatocarcinoma. Nat Commun 2013;4:2508.

18. Li Y, Luo S, Ma R, Liu J, Xu P, Zhang H, et al. Upregulation of cytosolic phosphoenolpyruvate carboxykinase is a critical metabolic event in melanoma cells that repopulate tumors. Cancer Res 2015;75:1191–6.

19. Luo S, Li Y, Ma R, Liu J, Xu P, Zhang H, et al. Downregulation of PCK2 remodels tricarboxylic acid cycle in tumor-repopulating cells of melanoma. Oncogene 2017;36:3609–17.

20. Ma R, Ji T, Zhang H, Dong W, Chen X, Xu P, et al. A Pck1-directed glycogen metabolic program regulates formation and maintenance of memory CD8(+) T cells. Nat Cell Biol 2018;20:21–27.

21. Liu J, Tan Y, Zhang H, Zhang Y, Xu P, Chen J, et al. Soft fibrin gels promote selection and growth of tumorigenic cells. Nat Mater 2012;11:734–41.

22. Liu Y, Liang X, Dong W, Fang Y, Lv J, Zhang T, et al. Tumor-repopulating cells induce PD-1 expression in CD8(+) T cells by transferring kynurenine and AhR activation. Cancer Cell 2018;33:480–94.

23. Liu Y, Lv J, Liu J, Liang X, Jin X, Xie J, et al. STAT3/p53 pathway activation disrupts IFN-β-induced dormancy in tumor-repopulating cells. J Clin Invest 2018;128:1057–73.

24. Long CP, Antoniewicz MR. High-resolution (13)C metabolic flux analysis. Nat Protoc 2019;14:2856–77.

25. van den Beucken T, Koch E, Chu K, Rupaimoole R, Prickaerts P, Adriaens M, et al. Hypoxia promotes stem cell phenotypes and poor prognosis through epigenetic regulation of DICER. Nat Commun 2014;5:5203.

26. Kim H, Lin Q, Glazer PM, Yun Z. The hypoxic tumor microenvironment in vivo selects the cancer stem cell fate of breast cancer cells. Breast Cancer Res 2018;20:16.

27. Gunton JE. Hypoxia-inducible factors and diabetes. J Clin Invest 2020;130: 5063–73.

28. Lv J, Liu Y, Cheng F, Li J, Zhou Y, Zhang T, et al. Cell softness regulates tumorigenicity and stemness of cancer cells. EMBO J 2021;40:e106123.

29. Toledo-Guzmán ME, Hernández MI, Gómez-Gallegos ÁA, Ortiz-Sánchez E. ALDH as a stem cell marker in solid tumors. Curr Stem Cell Res Ther 2019;14: 375–88.

30. Matsumoto M, Pocai A, Rossetti L, Depinho RA, Accili D. Impaired regulation of hepatic glucose production in mice lacking the forkhead transcription factor Foxo1 in liver. Cell Metab 2007;6:208–16.

31. Zhang H, Tang K, Ma J, Zhou L, Liu J, Zeng L, et al. Ketogenesis-generated β-hydroxybutyrate is an epigenetic regulator of CD8(+) T-cell memory development. Nat Cell Biol 2020;22:18–25.

32. Mast JM, Kuppusamy P. Hyperoxygenation as a therapeutic supplement for treatment of triple negative breast cancer. Front Oncol 2018;8:527.

33. Ibrahim AA, Schmithals C, Kowarz E, Köberle V, Kakoschky B, Pleli T, et al. Hypoxia causes downregulation of dicer in hepatocellular carcinoma, which is required for upregulation of hypoxia-inducible factor 1α and epithelial-mesenchymal transition. Clin Cancer Res 2017;23:3896–905.

34. Discher DE, Mooney DJ, Zandstra PW. Growth factors, matrices, and forces combine and control stem cells. Science 2009;324:1673–7.

35. Chowdhury F, Huang B, Wang N. Cytoskeletal prestress: the cellular hallmark in mechanobiology and mechanomedicine. Cytoskeleton (Hoboken) 2021. doi: 10.1002/cm.21658. Epub ahead of print.

36. Tan Y, Tajik A, Chen J, Jia Q, Chowdhury F, Wang L, et al. Matrix softness regulates plasticity of tumour-repopulating cells via H3K9 demethylation and Sox2 expression. Nat Commun 2014;5:4619.

37. Liu Y, Liang X, Yin X, Lv J, Tang K, Ma J, et al. Blockade of IDO-kynurenine-AhR metabolic circuitry abrogates IFN-γ-induced immunologic dormancy of tumor-repopulating cells. Nat Commun 2017;8:15207.

38. Ma J, Zhang Y, Tang K, Zhang H, Yin X, Li Y, et al. Reversing drug resistance of soft tumor-repopulating cells by tumor cell-derived chemotherapeutic microparticles. Cell Res 2016;26:713–27.

39. Liu Y, Lv J, Liang X, Yin X, Zhang L, Chen D, et al. Fibrin stiffness mediates dormancy of tumor-repopulating cells via a Cdc42-driven Tet2 epigenetic program. Cancer Res 2018;78:3926–37.

40. Paszek MJ, Zahir N, Johnson KR, Lakins JN, Rozenberg GI, Gefen A, et al. Tensional homeostasis and the malignant phenotype. Cancer Cell 2005;8: 241–54.

41. Ondeck MG, Kumar A, Placone JK, Plunkett CM, Matte BF, Wong KC, et al. Dynamically stiffened matrix promotes malignant transformation of mammary epithelial cells via collective mechanical signaling. Proc Natl Acad Sci U S A 2019; 116:3502–7.

42. Clevers H. The cancer stem cell: premises, promises and challenges. Nat Med 2011;17:313–9.

43. Liu Y, Zhang T, Zhang H, Li J, Zhou N, Fiskesund R, et al. Cell softness prevents cytolytic T-cell killing of tumor-repopulating cells. Cancer Res 2021;81:476–88.

44. Weinberg SE, Sena LA, Chandel NS. Mitochondria in the regulation of innate and adaptive immunity. Immunity 2015;42:406–17.

45. Marquez J, Flores J, Kim AH, Nyamaa B, Nguyen ATT, Park N, et al. Rescue of TCA cycle dysfunction for cancer therapy. J Clin Med 2019;8:2161.

46. Pick E. The necessity of NEDD8/Rub1 for vitality and its association with mitochondria-derived oxidative stress. Redox Biol 2020;37:101765.

47. Schieber M, Chandel NS. ROS function in redox signaling and oxidative stress. Curr Biol 2014;24:R453–62.

48. Godet I, Shin YJ, Ju JA, Ye IC, Wang G, Gilkes DM. Fate-mapping post-hypoxic tumor cells reveals a ROS-resistant phenotype that promotes metastasis. Nat Commun 2019;10:4862.

49. Semenza GL. Hypoxia-inducible factors: coupling glucose metabolism and redox regulation with induction of the breast cancer stem cell phenotype. EMBO J 2017;36:252–9.

50. Dan Dunn J, Alvarez LA, Zhang X, Soldati T. Reactive oxygen species and mitochondria: a nexus of cellular homeostasis. Redox Biol 2015;6:472–85.

51. Sabharwal SS, Schumacker PT. Mitochondrial ROS in cancer: initiators, amplifiers or an Achilles' heel? Nat Rev Cancer 2014;14:709–21.

52. Kalyanaraman B, Cheng G, Hardy M, Ouari O, Bennett B, Zielonka J. Teaching the basics of reactive oxygen species and their relevance to cancer biology: Mitochondrial reactive oxygen species detection, redox signaling, and targeted therapies. Redox Biol 2018;15:347–62.

53. Petersen MC, Vatner DF, Shulman GI. Regulation of hepatic glucose metabolism in health and disease. Nat Rev Endocrinol 2017;13:572–87.

54. Vander Heiden MG, Cantley LC, Thompson CB. Understanding the Warburg effect: the metabolic requirements of cell proliferation. Science 2009; 324:1029–33.

55. Kim J, DeBerardinis RJ. Mechanisms and implications of metabolic heterogeneity in cancer. Cell Metab 2019;30:434–46.

56. Ivan M, Kondo K, Yang H, Kim W, Valiando J, Ohh M, et al. HIFalpha targeted for VHL-mediated destruction by proline hydroxylation: implications for O2 sensing. Science 2001;292:464–8.

57. Jaakkola P, Mole DR, Tian YM, Wilson MI, Gielbert J, Gaskell SJ, et al. Targeting of HIF-alpha to the von Hippel-Lindau ubiquitylation complex by O2-regulated prolyl hydroxylation. Science 2001;292:468–72.

58. Isaacs JS, Jung YJ, Mole DR, Lee S, Torres-Cabala C, Chung YL, et al. HIF overexpression correlates with biallelic loss of fumarate hydratase in renal cancer: novel role of fumarate in regulation of HIF stability. Cancer Cell 2005;8:143–53.

59. Robey RB, Hay N. Is Akt the "Warburg kinase"?-Akt-energy metabolism interactions and oncogenesis. Semin Cancer Biol 2009;19:25–31.

60. Dodd KM, Yang J, Shen MH, Sampson JR, Tee AR. mTORC1 drives HIF-1α and VEGF-A signalling via multiple mechanisms involving 4E-BP1, S6K1 and STAT3. Oncogene 2015;34:2239–50.